

CHALMERS
UNIVERSITY OF TECHNOLOGY

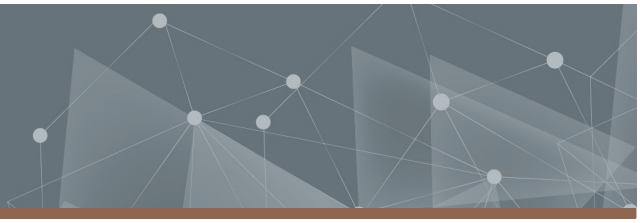

# Investigating Isotope Patterns Using Fourier Transform Ion Cyclotron Resonance Mass Spectrometry

Master's Thesis in Materials Chemistry

NATALIA LUGOWSKA

DEPARTMENT OF CHEMISTRY AND CHEMICAL ENGINEERING

CHALMERS UNIVERSITY OF TECHNOLOGY
Gothenburg, Sweden 2026
www.chalmers.se

Master's thesis 2026

# Investigating Isotope Patterns Using Fourier Transform Ion Cyclotron Resonance Mass Spectrometry

NATALIA LUGOWSKA




CHALMERS
UNIVERSITY OF TECHNOLOGY

Department of Chemistry and Chemical Engineering
*Division of Chemistry and Biochemistry*
Chalmers University of Technology
Gothenburg, Sweden 2026

Investigating Isotope Patterns Using Fourier Transform Ion Cyclotron Resonance Mass Spectrometry
NATALIA LUGOWSKA

© NATALIA LUGOWSKA, 2026.

Supervisor and Examiner: Per Malmberg, Department of Chemistry and Chemical Engineering

Master's Thesis 2026
Department of Chemistry and Chemical Engineering
Division of Chemistry and Biochemistry
Chalmers University of Technology
SE-412 96 Gothenburg
Telephone +46 31 772 1000

Typeset in LaTeX
Printed by Chalmers Reproservice
Gothenburg, Sweden 2026

Investigating Isotope Patterns Using Fourier Transform Ion Cyclotron Resonance Mass Spectrometry

NATALIA LUGOWSKA
Department of Chemistry and Chemical Engineering
Chalmers University of Technology

## Abstract

The evolution of high resolution mass spectrometry has opened a path to analysis of highly complex samples, with an unrivaled accuracy. As such, atomic-level differences can be resolved, providing the determination of exact masses, elemental compositions and importantly, isotopic contributions. This study investigated the use of a high resolution mass spectrometer, Fourier transform ion cyclotron resonance mass spectrometry (FT-ICR MS), for analysis of isotope patterns in complex biological samples, with matrix assisted laser desorption/ionization (MALDI) as an ion source. The work focused on collected mass spectra of two cyanobacteria strains, namely *Synechocystis* sp. PCC 6803 and *Cyanothece* sp. PCC 7425. The aim was therefore to evaluate whether MALDI FT-ICR MS could be used to characterize isotope patterns and isotopic fine structures.

Principal component analysis showed that *Synechocystis* and *Cyanothece* were chemically distinguishable, although they contained substantial overlap. After optimization of mass spectra acquisition, a data analysis approach to computing isotope patterns and isotopic fine structures was developed. The algorithm was based on the input of molecular formulas, that were subsequently picked out and found in raw MS data files. The isotopes and individual isotope contributions were computed, and confirmed using three criteria for validation. The clearest isotope patterns were obtained for the chlorophyll *a* derivative pheophytin *a*, which was used as an example peak for further isotope analysis. Overall, a number of analyte molecules showed strong agreement with theoretical isotope patterns. Analysis of the isotopic fine structures also showed that MALDI FT-ICR MS resolved contributions from not only carbon, but also nitrogen, magnesium, sulfur and oxygen.

The results demonstrated that MALDI FT-ICR MS can resolve isotope patterns and fine structure information from cyanobacterial spectra. At the same time, the study showed that identification of the isotopes depend on mass resolution, peak overlap and the presence of closely spaced ions. The workflow is thus most effective when a comprehensive interpretation is based on data analysis combined with manual spectral examination.

Keywords: mass spectrometry, isotopes, isotope ratio, FT-ICR, MALDI

## Acknowledgements

I would like to express a sincere thank you to my supervisor and examiner Per Malmberg. This project has been highly rewarding and a great learning experience for me. I would also like to thank Caroline Lööf and everyone else in Per Malmberg's group for their continuous support during this project.

A special thank you to Emma Hammarlund from Lund University, as well as Nicole Posth from the University of Copenhagen for providing the samples.

Lastly, I want to thank the Department of Chemistry and Chemical Engineering, and specifically the Division of Chemistry and Biochemistry, for the opportunity to utilize the facilities and for creating a great work environment.

Natalia Lugowska, Gothenburg, May 2026

# List of Figures


2.1 Simplified depiction of MALDI ionization mechanism. Adapted from [10]. . 4
2.2 Three common matrices for MALDI. . . . . 5
2.3 Simulated display of two methods of determining resolution. . . . . 7
2.4 Visualization of ion motion and detection in FT-ICR. . . . . 7

4.1 Illustration of sample mounting on target plate. . . . . 15

5.1 Spectra from measurements with three different concentrations. The top spectra is the concentration of 1 mg/ml, followed by 2 mg/ml and 10 mg/ml below. . . . . 18
5.2 Spectra collected using matrix compound CHCA compared to DHB. . . . . 19
5.3 Variation in intensity and number of peaks with increasing laser power. . . 20
5.4 Visualization of increased resolution in a single peak. The red dotted line indicates the theoretical m/z value. . . . . 21
5.5 Acquired mass spectra for a selected monoisotopic peak, depending on acquisition parameters 2M, 4M, 8M and 16M. . . . . 22
5.6 Chemical structure of chlorophyll-*a*. . . . . 23
5.7 PCA score plot for two cyanobacteria strains *Cyanothece* and *Synechocystis*, with three cultures each. . . . . 25
5.8 Visualization of PCA distance plotfor two cyanobacteria strains *Cyanothece* and *Synechocystis*, with three cultures each. . . . . 26
5.9 PCA loading plot for cyanobacteria strains *Cyanothece* and *Synechocystis*. . 27
5.10 Simulated spectra of [M+Na]+ region for pheophytin *a*. . . . . 30
5.11 Reproducibility test for intensity ratio of carbon isotope contributions in $M + 1$. . . . . 31
5.12 Isotopic fine structure comparison between theoretical pattern and found observed values, for $M + 1$ peak of pheophytin. . . . . 32
5.13 Isotopic fine structure comparison between theoretical pattern and found observed values, for $M + 2$ peak of pheophytin. . . . . 33
5.14 Isotopic fine structure comparison between theoretical pattern and found observed values, for $M + 1$ peak of SQDG 34:4. . . . . 33
5.15 Isotopic fine structure comparison between theoretical pattern and found observed values, for $M + 2$ peak of SQDG 34:4. . . . . 34

A.1 Overview of processed spectra with varying laser power. . . . . I

# List of Tables


3.1 Natural isotopic abundances of common isotopes. . . . . 10
3.2 Mass shifts between light and heavy isotopes of common elements [36]. . . . 12

5.1 Calculated approximate resolutions depending on acquisition parameters 4M, 8M and 16M. . . . . 21
5.2 Observed mass errors for pheophytin *a* peaks at different transient sizes. . . 22
5.3 Expected target compounds used for isotope analysis. . . . . 24
5.4 Occurrence of selected PCA-associated peaks in *Cyanothece* and *Synechocystis*. . . . . 27
5.5 Mean sum-normalized intensities for selected peaks with similar occurrence in *Cyanothece* and *Synechocystis*. Intensities are expressed as percentages of the total normalized spectral signal. . . . . 28
5.6 Mass accuracies for select validated parent ions. . . . . 29
5.7 Observed and expected combined isotope intensities for pheophytin *a* adducts. 30

# Contents


**1 Introduction** **1**
- 1.1 Aim and Objectives . . . 2
- 1.2 Limitations . . . 2

**2 Mass Spectrometry** **3**
- 2.1 Ionization Methods . . . 3
  - 2.1.1 Matrix-Assisted Laser Desorption/Ionization . . . 4
    - 2.1.1.1 Matrix and Laser Effects . . . 5
- 2.2 Mass Analyzers . . . 6
  - 2.2.1 Fourier Transform Ion Cyclotron Resonance . . . 7
    - 2.2.1.1 Space Charge Effects . . . 9

**3 Stable Isotopes** **10**
- 3.1 Natural Abundance . . . 10
- 3.2 Isotope Ratios . . . 11
- 3.3 Isotopes and Mass Spectrometry . . . 11

**4 Methods** **14**
- 4.1 Materials and Preparation . . . 14
- 4.2 Ionization . . . 14
  - 4.2.1 Laser and Matrix Parameters . . . 15
- 4.3 Data Collection . . . 15
  - 4.3.1 Calibration . . . 16
  - 4.3.2 Acquisition Parameters . . . 16
- 4.4 Multivariate Analysis . . . 16
- 4.5 Isotope Analysis . . . 17

**5 Results and Discussion** **18**
- 5.1 Method Development . . . 18
  - 5.1.1 Matrix Selection . . . 18
  - 5.1.2 Laser Optimization . . . 19
  - 5.1.3 Improving Resolution . . . 20
- 5.2 General Observations . . . 23
- 5.3 Multivariate Analysis . . . 24
- 5.4 Isotope Analysis . . . 28
  - 5.4.1 Isotope Patterns . . . 29
  - 5.4.2 Isotopic Fine Structure . . . 31

**6 Conclusions and Future Outlook** **36**

**References** **37**

**A Appendix** **I**

# 1
# Introduction

The chemical composition of natural and biological materials carries information about their origin, history, and transformation. Isotope analysis provides a way to access this information through the ratio of the abundance of heavy and light isotopes, such as $^{13}C/^{12}C$, $^{15}N/^{14}N$, and $^{18}O/^{16}O$ [1]. The isotope ratios can change during physical, chemical and biological processes, and are visualized by measurable variations in the isotopic patterns [2]. Monitoring changes in the patterns may reflect how a material has been affected, such as how it was formed, altered or exposed to different conditions. Hence, isotopic patterns can offer additional information in biomaterials by revealing transformations at the atomic level, thus providing another layer of diagnostic information. Consequently, characteristic patterns in isotope ratios can be observed, reflecting the isotopic fingerprint of a sample. Analysis of shifts in isotope ratios is therefore an important approach for developing isotope-based biomarkers.

Studying isotopes is a widely used application across many disciplines. For example, oxygen isotopes in ocean water and ice is used to simulate past climates and ice ages [3]. Because $^{16}O$ evaporates more easily, while $^{18}O$ condenses faster, lower concentrations of $^{16}O$ in ice layers indicate colder climate conditions. Stable isotope analysis can also be used for food authentication, where isotopic fingerprints can verify both the origin as well as the purity of food products. An example is honey, where the incorporation of sugar is often used to increase product volume [4]. By analyzing $^{13}C$ ratios in the honey, differentiation between real honey and added sugars can be determined. This is because plants with different metabolic pathways have specific carbon isotope values, which are reflected in the sugar.

Biological samples are complex, containing a wide range of molecular species in cells, tissues, metabolites and many other biomolecules. To analyze isotopic patterns in them may express valuable information about biological processes, however, interpreting these patterns requires analytical techniques capable of resolving subtle mass differences. Typically, isotope ratios are measured using a specialized mass spectrometry technique known as isotope ratio mass spectrometry (IRMS) [5]. IRMS is well established and highly precise for determining isotope ratios of light elements. However, the sample preparation is generally extensive and often includes combustion or pyrolysis, converting the sample into simple gases before analysis. Although this approach is highly effective for bulk isotope-ratio measurements, it removes most of the original biological and molecular composition of the sample. For biological samples, this may result in the loss of important molecular information.

In recent years, the development of analytical techniques with high sensitivity and mass

accuracy has increased. The most prominent are high resolution mass spectrometers (HRMS), which have become important tools for chemical analysis [6]. Some of the most widely used HRMS instruments are Orbitrap and Fourier transform ion cyclotron resonance mass spectrometry (FT-ICR MS), which both determine mass-to-charge ratios from ion frequencies. Orbitrap instruments offer excellent mass accuracy and high resolving power, while having faster acquisition rates and a more compact instrument design. On the other hand, FT-ICR MS provides incomparably high mass resolution and mass accuracy, allowing the analysis of complex mixtures with little prior simplification [7]. The high resolving power of the technique makes it possible to distinguish closely spaced signals that may overlap in lower resolution instruments, which makes it ideal for isotope analysis.

## 1.1 Aim and Objectives

The aim of the project is to investigate and identify isotope patterns in different organisms using ultra-high resolution mass spectrometry, specifically FT-ICR MS with matrix-assisted laser desorption/ionization (MALDI), as the primary ion source.

Thus, the main objectives consist of: i) developing a method for retrieving isotope patterns in FT-ICR MS, ii) determining isotope ratios in select biological samples, iii) optimizing matrix and laser parameters for MALDI, and iv) quantifying results for data analysis.

## 1.2 Limitations

The project does not involve the preparation and growth of bacterial samples but will instead be provided by collaborators. Hence, the influence over certain parameters such as culture medium and extraction methods is limited, as well as any potential variability in the preparation stage.

The main focus of this study is on mass spectrometry and data analysis. Thus it is not aiming to understand the biological and mechanistic processes, but is instead limited to the analytical perspective of detecting and quantifying isotopic patterns.

# 2

# Mass Spectrometry

Mass spectrometry (MS) is an analytical technique used to identify molecules based on their mass-to-charge (m/z) ratio. In the mass spectrometer, the analyte molecules are ionized and separated according to their m/z values. Subsequently, they are detected and produce a mass spectrum. The spectrum then provides information such as the molecular masses as well as the relative abundances of the ions present in the sample.

There are a variety of mass spectrometers, that differ in attributes such as the ionization method, the mass detector and the resolution. The choice of set-up is thus adjusted to suit the sample. For studies of complex samples, high accuracy and mass resolution are typically required. An instrument that provides such ability is Fourier transform ion cyclotron resonance mass spectrometry (FT-ICR MS) which offers high resolving power and mass accuracy [8]. Thus, this chapter introduces the basic principles of mass spectrometry, with a focus on FT-ICR MS.

## 2.1 Ionization Methods

The first step of any mass spectrometry analysis is the ionization, where the sample is converted to gas-phase ions. Different ion sources can be utilized based on the nature of the analyte, and has significant impact on the identification process [9]. There are various ionization methods and sources, and they can be roughly separated into hard and soft ionization. This depends on the amount of internal energy that is transferred during the process [10].

Hard ionization methods, such as electron ionization, are highly energetic, which results in substantial fragmentation of the sample. Additionally, hard ionization typically require the sample to be introduced in gas-phase, which limits the applicability of the technique to smaller molecules that possess sufficient volatility [8]. On the other hand, there are analytes that lack the vapor pressure or thermal stability, which cannot be ionized as such. Thus, soft ionization methods developed for both liquid- and solid state samples are employed instead, which involve lower internal energy [11]. For liquid-phase ion sources, e.g. electrospray ionization and atmospheric pressure chemical ionization, the analyte is introduced in solution and nebulized to form droplets. Subsequently, the solvent evaporates and expedites the ionization reactions, leading to the formation of gas-phase ions. For many solid-state samples, ionization techniques that employ a matrix are useful. The matrix absorbs energy and facilitates the desorption of the analyte into the gas phase, while promoting ion formation and reducing fragmentation.

### 2.1.1 Matrix-Assisted Laser Desorption/Ionization

One common ion source is matrix-assisted laser desorption/ionization (MALDI), which is based on photoionization by irradiation with a laser [9]. MALDI is suitable for molecules that are otherwise hard to ionize, such as larger biomolecules or compounds with lower volatility. This is due to the analyte being embedded in a matrix, which protects it from direct interaction with the laser, as well as enables desorption from the solid state. Because fragmentation is limited and predominantly singly charged ions are produced, MALDI is considered a soft ionization technique [12].

When preparing for analysis the analyte is initially dissolved in a matrix solution, and then allowed to co-crystallize and dry. A pulsed laser beam is then used to ablate the surface. This process involves a rapid phase transition that can eject a mixture of matrix-analyte clusters, neutral molecules and charged species into the gas phase. The resulting plume expands away from the surface, carrying both matrix and analyte ions. Ion formation occurs during and after ablation, although the exact mechanisms remain undetermined [10]. A generalized workflow of the MALDI mechanism is illustrated in figure 2.1 below.

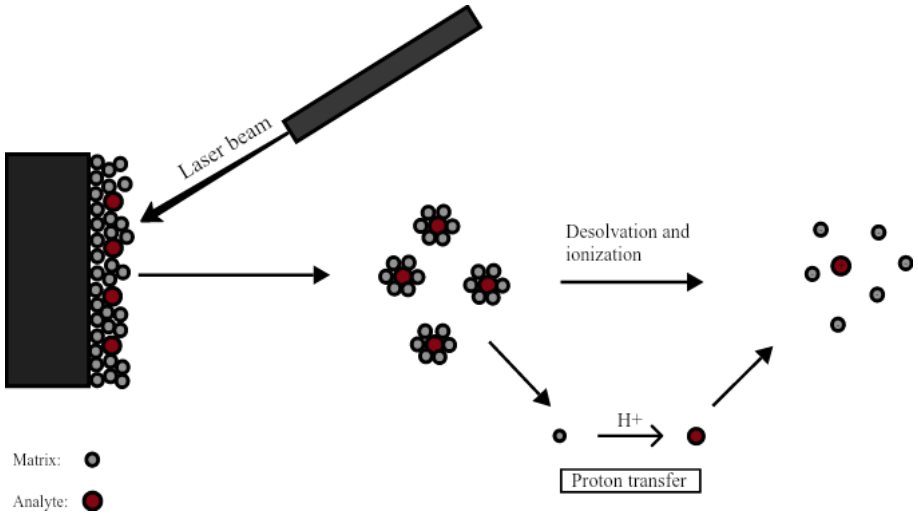


**Figure 2.1:** Simplified depiction of MALDI ionization mechanism. Adapted from [10].

As mentioned, the mechanism of the ionization reactions is not completely elucidated because the processes are rapid. However, there are widely accepted theories to explain it. As such, MALDI ionization can be explained as the result of a two-step process, primary and secondary ionization [13]. These stages are not independent, but are rather coupled in the environment created by the laser ablation and the evolving plume.

The primary ionization depends on the function of the matrix, which is to absorb laser energy and distribute it in the lattice. Importantly, the phase transition mechanism is debated regarding the origin and nature of the ion formation. They may arise from electronically excited states in the solid, from ion pair separation during ablation or from reactions at the solid–gas interface [12].

There are some proposed models which describe the process of primary ionization. One of the oldest is the "Lucky Survivor" model, that suggests that preformed ions which exist in solution remains in the solid state [14]. Thus, the ions that are "survivors" from neutralization, are simply released as they are during the desorption. However, isolated ions

are energetically unfavorable in solid materials, making this model less likely.

Some other alternatives include mechanical charge separation as a result of breaking up the crystal lattice, or thermal ionization which indicates that the heat of the plume may lower the energy required for ion separation [15]. Lastly, non-thermal mechanisms based on electronic excitation of the matrix are often postulated. Absorption of photons excites matrix molecules and causes sharp increases in local energy accumulation [10],[16]. Hence, the primary formation of ions are derived from the matrix, and subsequently plays a central role in the secondary ionization.

During the plume expansion, primary ions react with neutral species or other ions, which constitutes the secondary ionization. The majority of ions later detected in the mass spectrum are ions formed during this stage [13]. Perhaps the most abundant contribution stems from ion formation due to proton transfer from matrix ions to analyte molecules. If the matrix is denoted as M and the analyte as A, the general chemical reaction is expressed as equation 2.1 below.

$$MH^+ + A \rightleftharpoons M + AH^+ \tag{2.1}$$

Additionally, reactions can occur via similar pathways by electron transfer or metal cationization, which is highly dependent on the matrix and composition of the sample [17]. Cation adducts are commonly observed in samples which have low proton affinity, or for example in biological samples which naturally contain salts.

#### 2.1.1.1 Matrix and Laser Effects

A critical part which determines the efficiency of MALDI, is the combination of the matrix attributes and the laser parameters. For UV MALDI, the wavelength of the laser must match the absorption spectrum of the matrix to ensure photon absorption. Two common UV-lasers for MALDI instruments are either nitrogen lasers with wavelength 337 nm, or Nd:YAG lasers at 355 nm. Typical matrices are sinapinic acid (SA), 2,5-dihydroxybenzoic acid (DHB) and $\alpha$-cyano-4-hydroxycinnamic acid (CHCA), which all readily absorb UV-light at both 337 nm and 355 nm.

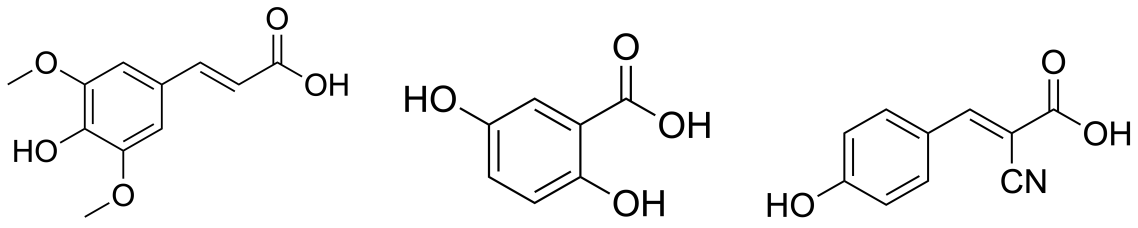


**(a)** Sinapinic acid.

**(b)** 2,5-dihydroxybenzoic acid.

**(c)** $\alpha$-cyano-4-hydroxycinnamic acid.

**Figure 2.2:** Three common matrices for MALDI.

The matrix does not only serve as a medium, but also provides an environment that further supports ion formation and desorption [12]. Matrices containing acidic functional groups undergo proton transfer reactions more readily, and can donate protons more efficiently. Differences in molecular structure of the matrix also affect how it absorbs laser energy. The presence of functional groups such as hydroxyl, carboxyl and cyano groups

enables easier electronic excitation upon laser irradiation. Additionally, matrix selection may vary according to the analyte molecules. For example, larger biomolecules require lower laser energy to minimize fragmentation, thus placing higher demands on homogenous co-crystallization. Smaller molecules such as peptides typically have lower sensitivity in those aspects.

The laser parameters have a significant influence on the desorption of ions and the expansion of the plume. The most important is the laser fluence, the total laser energy depositied per unit area [18]. The laser fluence must be sufficient enough to induce ablation, which is called the threshold fluence. However, if the laser energy is too large it may instead cause fragmentation or decrease resolution. As such, the laser energy along with the laser spot size must be optimized to the sample. The spot size determines the surface area and affects the local fluence in each laser shot [12]. If the laser energy remains fixed but the spot size decreases, the laser fluence will increase. A larger spot distributes the energy over a bigger area, but consequently ablates a larger portion of the sample. Other parameters include the number of laser shots and the frequency of laser pulses, which should be optimized depending on the sample.

## 2.2 Mass Analyzers

Following the ion source is the mass analyzer and detector, where the ionized sample is separated and measured depending on their mass-to-charge ratio. The mass spectrum is the result of the abundance of ions as a function of their m/z [19]. Thus, the most critical part of mass spectrometry is the mass analyzer's ability to resolve ions by their mass, serving as the basis for mass spectral analysis.

There are a number of available mass analyzers which differ in aspects such as resolution, accuracy and their suitability with different ion sources. Generally, mass analyzers separate or distinguish ions based on their behavior in electric and magnetic fields. Some analyzers separate ions by kinetic energy, such as as in time-of-flight instruments. Magnetic sector instruments separate ions based on the curvature of their paths in a magnetic field. Quadrupoles and ion traps instead use radiofrequency (RF) and direct-current (DC) electric fields to confine ions. There are also frequency based mass analyzers, such as Fourier transform ion cyclotron resonance and Orbitrap instruments, which instead determine m/z from the frequencies of ion motion.

The mass resolving power refers to the mass analyzer's ability to resolve and differentiate signals between two adjacent ions with a small mass difference [20]. It is typically defined as $R = m/\Delta m$ where $\Delta m$ is the smallest mass difference between two peaks. When resolving two peaks with the same nominal mass, $\Delta m$ is based on the valley between the peaks. The peaks are considered resolved if the valley intensity is at most equal to 10% of the lower intensity peak [10]. However, it is also possible to measure resolution in isolated peaks, using the width of the single peak. Thus, $\Delta m$ is based on the full width at half maximum (FWHM), which is at 50% of the maximum intensity. In figure 5.3 a visualization of both resolution methods is displayed.

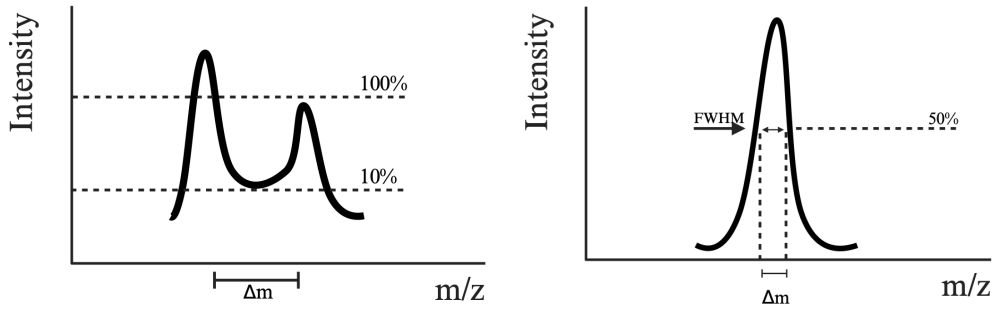


**(a)** 10% valley **(b)** FWHM

**Figure 2.3:** Simulated display of two methods of determining resolution.

Mass accuracy of a mass spectrometer refers to the accuracy with which the mass analyzer measures m/z compared to a theoretical value. The differences are often small, and is typically expressed in ppm. Hence, high mass accuracy is indicated by a low ppm error. Mass accuracy is dependent on the resolution power of the instrument, and varies between different analyzers.

### 2.2.1 Fourier Transform Ion Cyclotron Resonance

Fourier transform ion cyclotron resonance (FT-ICR) is a mass analyzer which determines m/z values of ions based on their ion cyclotron motion, in an applied magnetic field. FT-ICR mass spectrometry provides extremely high resolution and mass accuracy, making it ideal for measurements that require such resolving power. The general setup consists of a superconducting magnet, where a cylindrical ion trap is mounted inside, called an ICR cell.

The ICR cell is comprised of two excitation plates and two detection plates as the cylindrical walls, as well as two trapping electrodes on the ends of the cell [21]. An uniform magnetic field (B) is applied along the z-axis, trapping the ions radially, while a DC electric field on the endcap electrodes confines the ions axially, see figure 2.4. Hence, the ICR cell acts as a Penning trap, where the magnetic field forces the ions to circulate, inducing cyclotron motion, while the electric field prevents the ions from escaping.

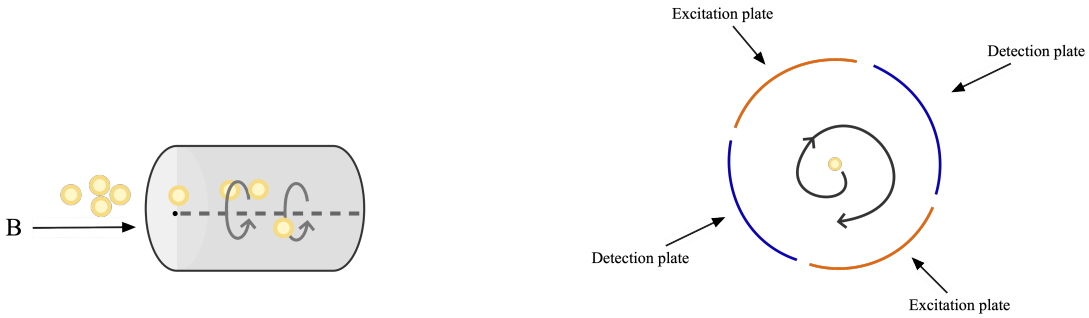


**(a)** Cyclotron motion of ions in ICR cell.

**(b)** Placements of plates in ICR cell.

**Figure 2.4:** Visualization of ion motion and detection in FT-ICR.

In FT-ICR, ion motion is governed by the forces that arise from electromagnetic fields,

which are generated by applied electric potentials and currents [22]. In the ICR cell, the DC electric field is used for axial trapping, while the magnetic field confines the ions radially. RF electric fields are then used for ion excitation, where the alternating electric potential produces a time-dependent electric field.

The force on a charged particle due to applied electric and magnetic fields is called the Lorentz force. In FT-ICR, this force makes ions undergo cyclotron motion in the applied magnetic field. The general form is expressed as

$$\mathbf{F} = q\left(\mathbf{E} + \mathbf{v} \times \mathbf{B}\right) \tag{2.2}$$

where $\mathbf{E}$ is the electric field, $\mathbf{B}$ is the magnetic field, and $\mathbf{v}$ is the particle's velocity. The electric field component accelerates the ion, while the magnetic field component curves the ion's trajectory. The magnetic component of the Lorentz force, shown in equation 2.3, acts perpendicular to the ion's velocity.

$$F_M = qvB \tag{2.3}$$

This force bends the ion path in a circular motion, thus acting as a centripetal force, as in equation 2.4.

$$F = \frac{mv^2}{r} \tag{2.4}$$

As such, an ion's path in a magnetic field can be described as:

$$qvB = \frac{mv^2}{r} \tag{2.5}$$

Through equation 2.3 the angular cyclotron frequency can be derived as,

$$\omega_c = \frac{qB}{m} \tag{2.6}$$

or in linear frequency form as:

$$f_c = \frac{qB}{2\pi m} \tag{2.7}$$

Importantly, this shows that the frequency is independent from the velocity of the ion, making the FT-ICR a frequency dependent instrument.

In addition to the primary motion, i.e the cyclotron frequency as described in equation 2.6, there are two other frequencies that are functions of m/z. They are magnetron motion, which is a small frequency drift around the center of the cell, as well as axial oscillation between the trapping plates [23]. Both of them are induced by the applied electric field, and are typically disregarded as they have significantly lower frequencies than the cyclotron motion.

Ion cyclotron resonance occurs when an external RF electric field is applied at the same frequency as the natural cyclotron frequency of an ion, through the excitation plates [24]. Each cyclotron frequency corresponds to a specific m/z value. However, before excitation the ions are confined close to the center of the ICR cell and only induces a weak signal at the detection plates. After excitation, the ions move in larger circular orbits and pass closer to the detection plates [25]. Their motion is detected as an image current on the

plates, which is recorded by the instrument. The recorded signal is called a free induction decay (FID) and it is measured in the time domain, referred to as a transient.

A Fourier transform is then applied to convert the time-domain transient into a frequency-domain spectrum as a function of signal intensity [24]. The measured frequencies are subsequently converted into m/z values using the relationship between cyclotron frequency and mass-to-charge ratio in equation 2.7, and calibrated. The resolving power of FT-ICR depends strongly on the duration of the detected transient, where longer detection times significantly increases the resolution [26]. Overall, the high resolving power and mass accuracy of FT-ICR arise from the precise measurement of ion cyclotron frequencies. Improvements in resolution for FT-ICR can generally be achieved by increasing the magnetic field strength and extending the transient acquisition time.

#### 2.2.1.1 Space Charge Effects

An important limitation of FT-ICR MS is space charge effects, which arises when larger numbers of ions are trapped in the ICR cell. At lower ion densities the interaction between ions are not significant. However, as the number increases, Coulumbic repulsion forces will incur additional electric fields between ions of similar m/z [27]. Therefore, the cyclotron frequencies may be altered which can cause mass shifts in the m/z values and thus decrease the mass accuracy. Additionally, highly abundant ions can perturb the motion of nearby ions, leading to peak broadening and reduced resolution [28].

The total impact of space charge effects depends on several parameters, especially the accumulation time and the total number of ions in the ICR cell. Increasing the accumulation time can improve resolution and signal intensity, but it also increases the probability of ion-ion interactions. On the other hand, too few ions result in weak signals and low signal-to-noise ratios. Thus, control of the ion population is essential for correct measurements, particularly when analyzing samples with large differences in ion abundances.

# 3

# Stable Isotopes

Most elements exist as a number of stable isotopes, i.e. non-radioactive isotopes that do not decay [29]. As isotopes differ in number of neutrons, there is a difference in nuclear mass. In nature, all materials appear as mixtures of stable isotopes in a similar way around the globe. However, isotopic compositions may vary slightly due to factors such as location or external impact. Thus, differences in chemical properties can be analyzed through isotopes, and provide information about the material including its history, origin or other chemical processes.

This chapter intends to introduce theory around stable isotopes, isotope effects and fractionation, as well as the use of mass spectrometry for analysis of the aforementioned.

## 3.1 Natural Abundance

The natural abundance of an element's stable isotopes refer to the mean abundance of the element across the Earth, where a common example is carbon [30]. The natural abundance of $^{12}C$ is approximately 98.9% and 1.1% for $^{13}C$ globally, whereas other carbon isotopes are radioisotopes that exist in trace amounts. Table 3.1 below presents the natural abundance of a selection of common elements [10].

**Table 3.1:** Natural isotopic abundances of common isotopes.

| Isotope | Relative Abundance (%) | Isotope | Relative Abundance (%) |
|---|---|---|---|
| $^{12}C$ | 98.90 | $^{32}S$ | 95.02 |
| $^{13}C$ | 1.10 | $^{33}S$ | 0.75 |
| $^{1}H$ | 99.985 | $^{34}S$ | 4.21 |
| $^{2}H$ | 0.015 | $^{36}S$ | 0.02 |
| $^{14}N$ | 99.63 | $^{24}Mg$ | 78.99 |
| $^{15}N$ | 0.37 | $^{25}Mg$ | 10.00 |
| $^{16}O$ | 99.76 | $^{26}Mg$ | 11.01 |
| $^{17}O$ | 0.04 | $^{35}Cl$ | 75.77 |
| $^{18}O$ | 0.20 | $^{37}Cl$ | 24.23 |
| $^{79}Br$ | 50.69 | $^{81}Br$ | 49.31 |

Within specific chemical or biological systems, these characteristic abundances deviate as a result of certain isotope effects. As isotopes have different mass, slight differences in mass dependent processes can be seen between them [31]. For example, the mass dif-

ference affects vibrational frequencies, bond energies, diffusion rates and reaction rates. Isotope effects are divided into two principal categories, kinetic and thermodynamic [30]. Kinetic isotope effects (KIE) occur as the cause of differing reaction rates between lighter and heavier isotopes, as lighter isotopes react more readily. Thermodynamic isotopic effects, or equilibrium effects, are instead related to how equilibrium constants of reversible reactions change when substituted with different isotopes [32].

Isotope effects often follow the classic mass dependent theory proportionally. However, sometimes deviations can be observed that cannot be explained by kinetic and equilibrium models [33]. Such variations are based on mass independent isotope effects instead, which occur due to photochemical and quantum-mechanical processes [31]. In photochemical reactions, light absorption causes excitation of electrons, where different forms of excited states are allowed depending on the molecular configuration. Substituting isotopes causes changes in the symmetry, resulting in different possible excitation states. Thus, the isotopic composition of the product changes based on quantum selectivity rather than mass [33]. They can also be induced by magnetic interactions, where isotopes with different spin will participate differently in, for example, radical reactions, significantly affecting the resulting isotopic composition [31].

## 3.2 Isotope Ratios

Measurements of stable isotope are typically expressed as isotope ratios instead of absolute abundances. The isotope ratio is the relative abundance of the isotopes, expressed as the ratio of the heavier isotope to the lighter, such as $R = \frac{^{18}\mathrm{O}}{^{16}\mathrm{O}}$ [1]. When comparing samples the differences are usually small, hence the isotope ratios are expressed using the $\delta$-notation,

$$\delta = \left( \frac{R_{\text{sample}}}{R_{\text{standard}}} - 1 \right) \times 1000 \text{ ‰} \tag{3.1}$$

where $R_{\text{sample}}$ is the measured isotope ratio in the sample and $R_{\text{standard}}$ is the isotope ratio in a reference material [34]. A positive $\delta$-value indicates that the sample is enriched in the heavy isotope relative to the standard, while a negative $\delta$-value indicates depletion.

Isotopic fractionation is the change in isotope ratio caused by chemical or physical processes, causing partitioning of heavy and light isotopes between samples. For example, the separation may be between compounds, biological material, phases or locations. The isotopic fractionation factor between two substances P and Q is expressed as

$$\alpha = \frac{R_P}{R_Q} \tag{3.2}$$

where $R_P$ is the isotope ratio of substance P and $R_Q$ the isotope ratio of substance Q [34].

## 3.3 Isotopes and Mass Spectrometry

In mass spectrometry, the isotopic composition of a molecule affects both the measured m/z values and their relative intensities. A molecule containing only the most abundant isotope of each element gives rise to the monoisotopic peak, commonly denoted as $M$. Molecules with the same elemental formula but different isotopic compositions are called

isotopologues. Each isotopologue will appear in a mass spectrum as systematic mass shifts from the monoisotopic signal. The isotope peaks are denoted as $M+1$, $M+2$ etc. when heavier isotopes are present.

Depending on the resolving power of the instrument, isotopes may appear as peaks or as isotope clusters [35]. High resolution mass spectrometers have the ability to distinguish between the exact mass shifts between heavy isotopes of different elements. For example, the mass difference between $^{13}C$ and $^{12}C$ is approximately 1.003355 Da, while the mass difference between $^{15}N$ and $^{14}N$ is approximately 0.997035 Da [36]. Thus, if the resolution between adjacent peaks is high enough, the separation of the peaks for e.g. $^{13}C$ and $^{15}N$ can be resolved, instead of appearing as a single $M+1$ peak. The distinction between isotopologes is called the isotopic fine structure (IFS). Below is a table containing the mass shifts between isotopes of some common elements.

**Table 3.2:** Mass shifts between light and heavy isotopes of common elements [36].

| Light Isotope | Heavy Isotope | Mass shift (Da) |
|---|---|---|
| $^{12}C$ | $^{13}C$ | 1.003355 |
| $^{1}H$ | $^{2}H$ | 1.006277 |
| $^{14}N$ | $^{15}N$ | 0.997035 |
| $^{16}O$ | $^{18}O$ | 2.004245 |
| $^{32}S$ | $^{33}S$ | 0.999387 |
| $^{32}S$ | $^{34}S$ | 1.995796 |
| $^{24}Mg$ | $^{25}Mg$ | 0.999593 |
| $^{24}Mg$ | $^{26}Mg$ | 1.998254 |
| $^{35}Cl$ | $^{37}Cl$ | 1.997050 |
| $^{79}Br$ | $^{81}Br$ | 1.997953 |

The intensity of the isotope peaks in a mass spectrum may be seen as comparable to the natural abundances of heavier isotopes. As an approximation, the relative intensity of the $M+1$ peak compared to the monoisotopic peak, $M$, can be described using the sum of all single isotopic substitutions. The following expressions are first-order approximations by truncating the full polynomial expansion of the theoretical isotope distribution [37], [38], [39]. In general form, this may be written as

$$\frac{I_{M+1}}{I_M} \approx \sum_x n_x f x \tag{3.3}$$

where $n_x$ is the number of atoms of element $x$ in the molecular formula and $f_x$ is the natural abundance of the heavy isotope contributing to the $M+1$ region, described in table 3.1. This expression shows that the relative intensity of the $M+1$ peak increases with the number of atoms of the relevant element. Typically, the dominant contribution is usually $^{13}C$ since carbon is highly abundant. On the other hand, contributions from other isotopes such as $^{2}H$, $^{15}N$, $^{17}O$ and $^{33}S$ may also be seen.

The $M+2$ region is more complex as it can be comprised of several different isotopic combinations. These include double substitutions of +1 isotopes of the same element, direct substitutions by isotopes with +2 Da difference, as well as mixed substitutions involving two different +1 isotopes. Thus, another general approximation for the relative

intensity of the $M+2$ peak can be written as:

$$\frac{I_{M+2}}{I_M} \approx \sum_x \binom{n_x}{2} f_x^2 + \sum_y n_y f_y + \frac{1}{2} \sum_{x,z} n_x f_x \, n_z f_z \tag{3.4}$$

The first term describes double +1 substitutions of the same element, such as $2 \times {}^{13}\mathrm{C}$. The second term represents +2 substitutions from e.g. ${}^{18}\mathrm{O}$ or ${}^{34}\mathrm{S}$. Lastly, the third term describes the mixed combinations such as ${}^{13}\mathrm{C} + {}^{15}\mathrm{N}$ or ${}^{13}\mathrm{C} + {}^{17}\mathrm{O}$.

As an example, a molecule containing carbon, hydrogen, and oxygen the $M+1$ peak may be approximated as

$$\frac{I_{M+1}}{I_M} \approx n_C f_{13C} + n_H f_{2H} + n_O f_{17O} \tag{3.5}$$

where $f_{13C}$, $f_{2H}$, and $f_{17O}$ denote the natural abundances of ${}^{13}\mathrm{C}$, ${}^{2}\mathrm{H}$, and ${}^{17}\mathrm{O}$, respectively.

Similarly, the $M+2$ peak for a molecule containing only carbon, hydrogen and oxygen can instead be approximated as

$$\begin{aligned} \frac{I_{M+2}}{I_M} \approx \binom{n_C}{2} f_{13C}^2 + \binom{n_H}{2} f_{2H}^2 + \binom{n_O}{2} f_{17O}^2 + n_O f_{18O} \\ + n_C f_{13C} \, n_H f_{2H} + n_C f_{13C} \, n_O f_{17O} + n_H f_{2H} \, n_O f_{17O} \end{aligned} \tag{3.6}$$

thus accounting for all possible isotope combinations. These expressions are simplified, but is useful for estimation of contributors to the $M+1$ and $M+2$ regions, as well as for comparison with experimental data.

In ultra-high-resolution mass spectrometers such as FT-ICR MS, isotopic fine structures can be resolved to distinguish individual contributions. However, even at high resolution, weaker isotope contributions may still overlap with stronger neighboring peaks. For this reason, interpretation of isotopic fine structure should be made with some caution.

# 4
# Methods

The project aims to investigate isotopes in biological samples using MALDI FT-ICR MS. As such, the experimental design consisted of i) sample and matrix preparation, ii) optimization of laser parameters, iii) acquisition of mass spectra and iv) statistical and computational data analysis of isotopic patterns. This chapter presents the workflow in greater detail.

## 4.1 Materials and Preparation

The primary biological material that was analyzed was cyanobacterial samples of the strains *Synechocystis* sp. PCC 6803 and *Cyanothece* sp. PCC 7425. For each strain, three independent cultures from different parent cultures respectively were prepared. The bacteria were grown in liquid culture medium and subsequently centrifuged and frozen. Approximately a week later the samples were freeze-dried, resulting in dry pellets.

The matrix compounds were $\alpha$-cyano-4-hydroxycinnamic acid (Sigma-Aldrich) and 2,5-dihydroxybenzoic acid (Sigma-Aldrich). For the matrix solution the solvents included acetonitrile (99.9 %, Sigma-Aldrich), Milli-Q® water (18.2 M$\Omega \cdot$ cm) and trifluoracetic acid (TFA, Acros Organics). The matrices were solved with 80:20 acetonitrile/water, with 0.1% TFA added, and prepared with the matrix concentration of 1 mg/ml, 2 mg/ml and 10 mg/ml respectively. The external calibrant used was red phosphorus (Sigma-Aldrich) solved in acetone (Thermo Scientific).

The instrument that was used to perform mass spectral analysis was a scimaX® (Bruker Daltonics), with a MALDI ion source using a Nd:YAG laser (355 nm). The scimaX® is equipped with a 7 T superconducting magnet.

## 4.2 Ionization

For the MALDI ion source the samples were mounted on a stainless steel target plate (MTP AnchorChip™, Bruker Daltonics), using the dried droplet method. Each sample was mixed with matrix solution in an approximate 1:1 ratio to a total volume of 10 $\mu$l. Using a micropipette, the sample-matrix solution was spotted on the target plate with 1 $\mu$l per spot. The spots were then left to dry and crystallize. A depiction of the MALDI mounting process is presented in figure 4.1 below.

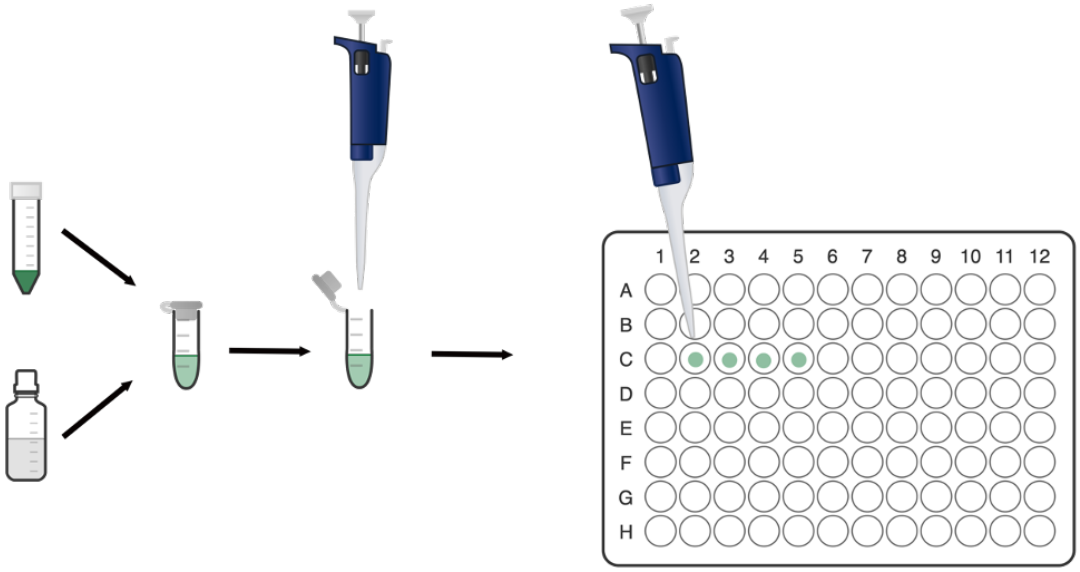


**Figure 4.1:** Illustration of sample mounting on target plate.

Following the crystallization, the target plate was subsequently introduced to the MALDI ion source.

### 4.2.1 Laser and Matrix Parameters

To optimize the ionization of the samples, several laser parameters were altered and compared, with the goal of high signal intensity as well as reproducible results. Hence, the main parameters that were optimized were the laser power and the laser focus (beam size). To evaluate the effect on the results, the peak intensities and the number of detected peaks were compared. During the measurements, all other parameters were kept constant to ensure that potential differences were attributed solely to changes in the laser settings.

Commonly used matrices for bacterial samples are CHCA and DHB, which were selected for evaluation in this project. The matrix solutions were prepared according to Section 4.1, with varying concentrations. Similarly to the laser settings, the varying factor was solely the matrix compound as well as the matrix concentration. However, the evaluation was mainly qualitative in nature and based on the spectral appearance. Particular regard was taken to minimizing the presence of matrix peaks in the spectrum, as well as the overall average signal intensities.

## 4.3 Data Collection

Following the ionization is the separation and detection of the ions m/z values in mass spectra. The general goal of data collection is to ensure a consistently high mass accuracy in addition to high peak resolution.

The general workflow of the spectral collection was to first optimize all parameters, including calibration, by collecting spectra and comparing them. Afterward, the developed

final method was then used to collect a minimum of ten replicates of each sample to be further analyzed.

### 4.3.1 Calibration

Prior to spectral acquisition the instrument was calibrated with an external calibration standard, consisting of red phosphorus (red P) dissolved in methanol. Red P does not require any addition of matrix to ionize efficiently and is effective for a broad mass range. Calibration spectra were collected with the intended laser parameters and mass range as for the sample measurements, to minimize potential deviations.

The characteristic peaks from the resulting spectrum were compared with a defined calibration peak list for red P. As such, a quadratic calibration function was fitted and then applied to all succeeding spectral collections. The mass accuracy of each calibration point was based on the mass error between the observed value and the reference value, in parts per million (ppm). The target value of the total standard deviation of the calibration was a value below 1 ppm.

### 4.3.2 Acquisition Parameters

The mass range for all sample measurements was m/z 50-1500, to ensure the inclusion of mostly smaller metabolites and keeping accurate calibration. The recorded transient time was alternated between 0.5-4 seconds to evaluate potential increases in peak resolution.

The number of scans was kept to one per measurement for the spectra that were collected for optimization of parameters. After the parameters were set, the measurements intended for isotope analysis were obtained with signal-averaged spectra of 100 scans to ensure statistical relevance, as well as to improve signal-to-noise ratios.

To reduce potential space charge effects the total ion count (TIC) was controlled for measurements with multiple scans, matching the TIC observed for the calibration. As such, the differences in TIC between each scan were reduced to $\pm 20\%$ of the calibration values.

## 4.4 Multivariate Analysis

For comparison of the spectral profiles, the FT-ICR MS data was first preprocessed using *mdatools* package in R [40], and used for multivariate analysis after. Preprocessing consisted of applying a Savitzky-Golay filter to smooth signals, asymmetric least-squares (ALS) baseline correction and sum normalization. An aligned feature table was generated from recurring peaks detected across the dataset and was then used for principal component analysis (PCA). PCA was used to examine differences between the spectra and to identify the m/z features contributing to the observed separation. It was also used to asses the reproducibility of replicates of measurements.

## 4.5 Isotope Analysis

After acquisition, all mass spectra were exported as raw profile spectra in the CSV file format, for further data analysis. All analyses was made using Python.

The workflow for the isotope analysis was based on the input of specific molecular formulas, henceforth called targets. For each sample a predefined target list contained plausible or expected compounds in the 50-1500 m/z range. The molecular parent ion was then searched and assigned as the highest-intensity peak within a search window of ±5 ppm around the theoretical mass value. For each target, theoretical masses for some common potential adducts [M+H]+, [M+Na]+, and [M+K]+ were also searched for.

To reduce the risk of assigning noise or overlapping peaks from other molecules, only candidates above a minimum intensity threshold were picked. The mass error of the parent ion was calculated as the difference between observed and theoretical m/z, and later expressed in parts per million. A parent ion was then picked if the absolute mass error was within 2.0 ppm of the theoretical value.

After assignment of a parent ion, the corresponding isotope peaks were examined in the $M+1$ and $M+2$ regions. For an isotope peak to be considered found, it was required to satisfy three conditions for validation. They were consistent in shift from the parent ion, had high mass accuracy and lastly plausible intensity. Then the expected isotope position was calculated theoretically, while the search window for the isotopes were shifted by the same ppm error offset as the previously picked parent ion. This ensured that isotope candidates were evaluated relative to the observed parent ion shift, rather than against the ideal theoretical mass. Secondly, the observed isotope peak had to be within 0.2 ppm in m/z, compared to this shifted theoretical position. Ultimately, the observed intensity ratio of the isotope and the monoisotopic ion had to be close to the expected ratio from natural isotopic abundance, to be considered valid.

To evaluate whether observed isotope intensities were chemically plausible, the experimental data was compared to theoretical isotope patterns. The full experimental isotope clusters were compared with the theoretical isotopic envelope generated by IsoSpecPy, which is a Python extension of IsoSpec2 which computes isotopic fine structures [41]. Experimental and theoretical peaks were then matched within the isotope cluster, and only validated matches were accepted.

To visualize the results, plots of experimental and theoretical isotope patterns were overlayed. In addition, summary tables were computed, containing parent ion matches, isotope assignments, fine structure candidates and the theoretical isotope profiles.

# 5

# Results and Discussion

This chapter presents the results obtained from the MALDI FT-ICR MS analysis of the investigated samples. To interpret the spectral data, the discussion is presented together with the results directly.

## 5.1 Method Development

### 5.1.1 Matrix Selection

For CHCA, three different concentrations of matrix compound were tested, 1 mg/ml, 2 mg/ml and 10 mg/ml.

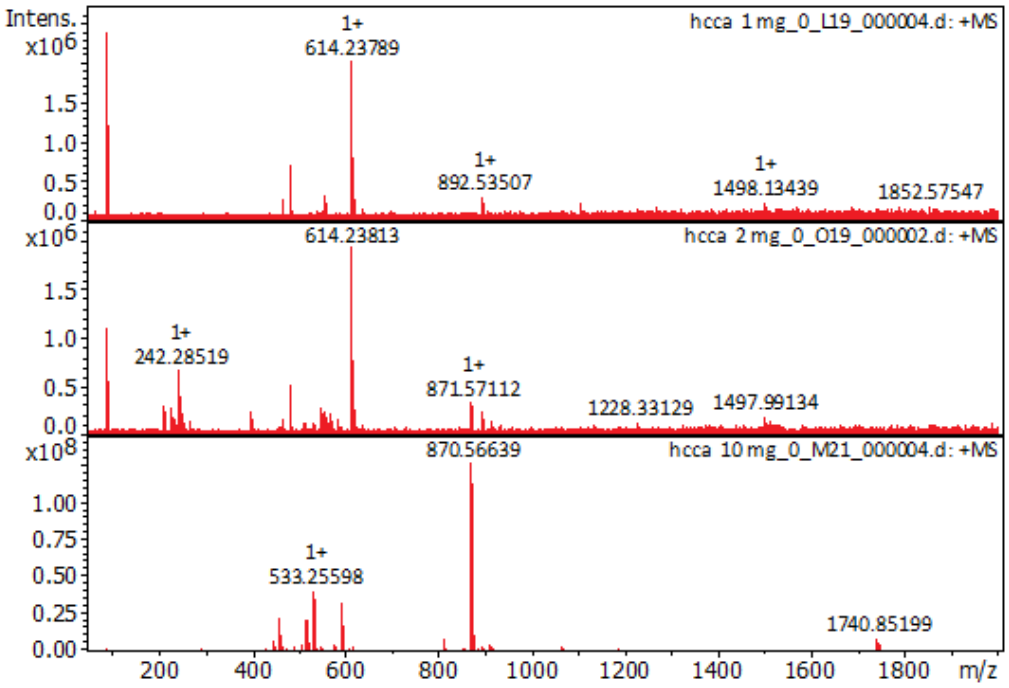


**Figure 5.1:** Spectra from measurements with three different concentrations. The top spectra is the concentration of 1 mg/ml, followed by 2 mg/ml and 10 mg/ml below.

The lowest concentration resulted in sparse spectra with low intensities. For 2 mg/ml, the overall number of peaks was greater, but a significant presence of matrix peaks dominated the spectra. The higher number of matrix peaks observed for 2 mg/ml CHCA compared to 10 mg/ml CHCA likely reflects the importance of an optimal ratio between analyte and matrix, which is integral for homogeneous crystallization. When crystallization is not

sufficient, the analyte signals may decrease due to analyte not being adequately incorporated, and the matrix being ionized instead. As such, the 10 mg/ml concentration resulted in suppression of matrix peaks, as well as an increase in overall analyte peak intensity. Figure 5.1 presents all three concentrations compared to each other.

Additionally, CHCA was compared briefly to DHB, both with the concentration of 10 mg/ml, to investigate any differences in peak intensity, broadening and fragmentation. See figure 5.2 below for the direct comparison.

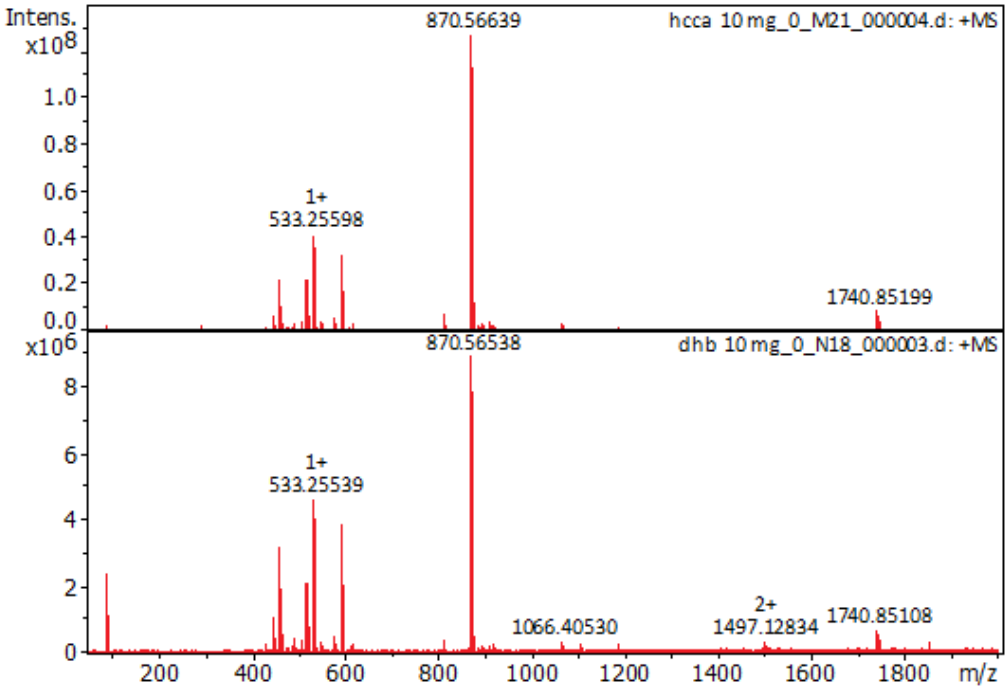


**Figure 5.2:** Spectra collected using matrix compound CHCA compared to DHB.

The resulting spectra were highly similar in pattern, but with lower total ion intensity for DHB. Therefore, the final choice for all further collection of mass spectra was 10 mg/ml CHCA.

### 5.1.2 Laser Optimization

The parameter that proved to have the greatest effect on the spectra was the laser energy, which in the instrument is expressed as laser power. The laser power can be chosen as a percentage of the maximum energy of the laser. The optimal value was chosen by analyzing the total number of peaks, the peak intensities and the overall appearance of the spectrum. The laser power was varied from 10-50%, and a full overview of processed and reconstructed spectra of each measurement is presented in figure A.1 in Appendix. Figure 5.3a below shows the effect of laser power on the intensity of the most intense signal in each spectrum, the base peak. Figure 5.3b shows the number of high intensity peaks, in processed spectra after smoothing and binning of raw profile data.

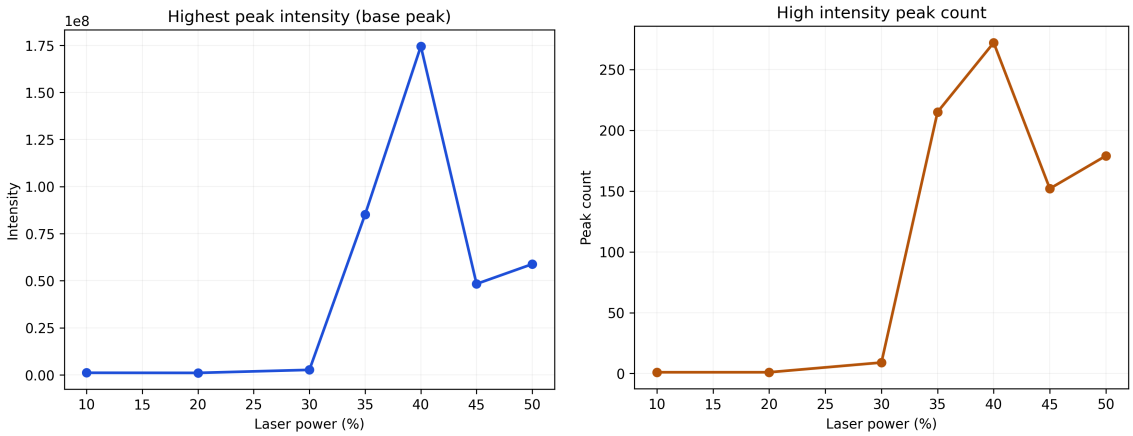


**(a)** Intensities of base peak.

**(b)** Number of high intensity peaks.

**Figure 5.3:** Variation in intensity and number of peaks with increasing laser power.

Together, the figures show that at the lowest settings for laser power, 10% and 20%, the spectra show almost no signals or clear peaks. At 30% laser power, there is a slight increase in signal intensity. However, the biggest change occurred between 30% and 35%, where both the base peak intensity and the peak count increased drastically. This was further pronounced for 40%, which produced the highest base peak intensity and the largest number of clearly distinguishable peaks. At 45% and 50%, the values still remained relatively high but both signal intensity and peak count decreased compared with the 40% setting. When visually inspecting the spectra acquired at 50% laser power. there is notably higher intensity contribution from signals at lower m/z. This may suggest that at higher laser energy settings, there is increased fragmentation of higher m/z ions, causing higher abundances of fragments with lower m/z. The final results thus showed that increasing the laser power improved the overarching spectral quality only up to a certain level. As such, the 40% laser power setting was determined to be the optimal choice.

The effect of laser focus was examined qualitatively by inspecting the spectra visually, as well as the sample spot after irradiation with the laser. Increasing the laser focus from the minimum value of 50 $\mu$m to 100 $\mu$m, resulted in much higher ablation of the sample spot, and left holes in the sample. Additionally, the spectra were distorted and overcrowded, even when the laser power was reduced. The total ion count (TIC) also increased an order of magnitude, from approximately $10^7$ to $10^8$, suggesting that the 100 $\mu$m focus ionized the sample too aggressively, and may overload the ICR cell. Therefore, the 50 $\mu$m focus was chosen as the more suitable setting for the final method.

### 5.1.3 Improving Resolution

An improvement in resolution was achieved by increasing the transient size between 4M, 8M and 16M. In the scimaX, these settings alter the recorded time domain transient i.e. the number of acquired data points, thus allowing more precise determination of ion cyclotron frequencies. Hence, improved mass resolving power was noted, but with the consequence of longer acquisition times as well as larger output files, which may reduce throughput efficiency. An example of the difference in resolution is presented in figure 5.4.

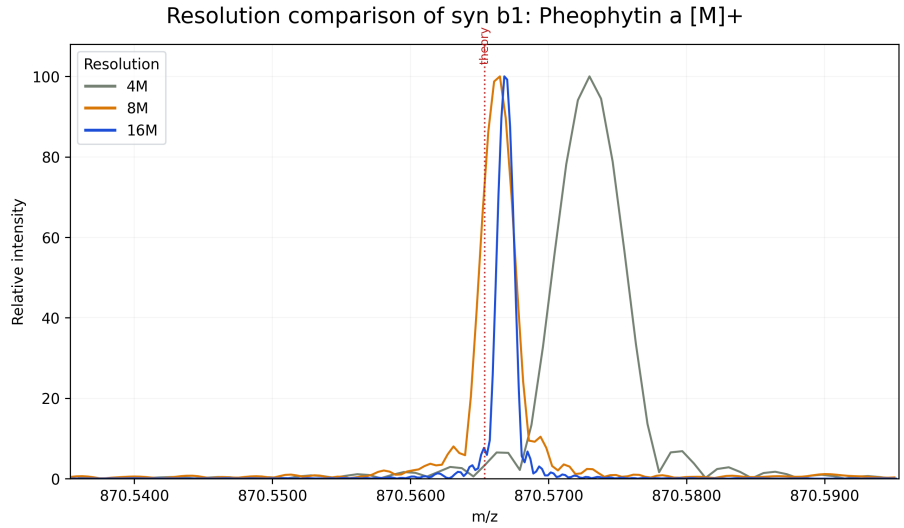


**Figure 5.4:** Visualization of increased resolution in a single peak. The red dotted line indicates the theoretical m/z value.

The comparison shows that increasing the transient size lead to narrower peaks. There is also a notable displacement from the theoretical value of the 4M peak, reflecting the result that broader peaks also may indicate less mass accuracy. The calculated values from processed spectra are presented in table 5.1 below.

**Table 5.1:** Calculated approximate resolutions depending on acquisition parameters 4M, 8M and 16M.

| **Transient Size** | **Approximate Resolution** |
|---|---|
| 4M | $1.58 \times 10^5$ |
| 8M | $3.18 \times 10^5$ |
| 16M | $6.24 \times 10^5$ |

Another example is presented directly from mass spectra in the scimaX software Data-Analysis of a monoisotopic peak at the acquisition modes 2M, 4M, 8M and 16M, in figure 5.5. The peaks are clearly narrower, thus providing more precise mass measurement as well as the possibility to distinguish between overlapping peaks.

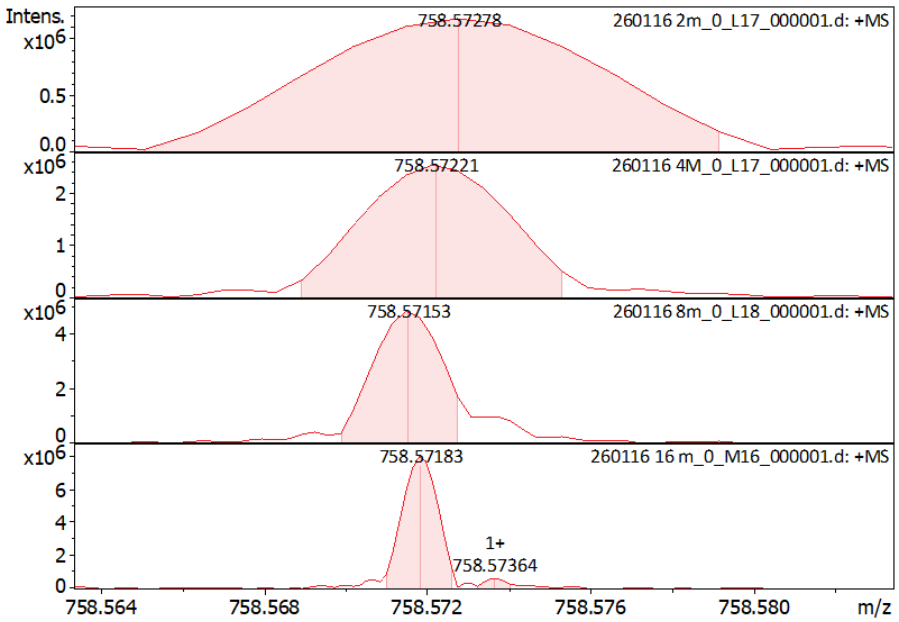


**Figure 5.5:** Acquired mass spectra for a selected monoisotopic peak, depending on acquisition parameters 2M, 4M, 8M and 16M.

In addition to the increase in resolving power, the mass accuracy also seemed to improve. For the example peak pheophytin *a* [M+H]+, the effect was observed as per table 5.2. For the 4M peak the mass error was about 7.1 ppm, while the 16M peak was within about 1.2 ppm of the theoretical mass. Thus, the main change from 4M to higher transient settings was not only narrower peaks, but also a more reliable identification of the compound.

**Table 5.2:** Observed mass errors for pheophytin *a* peaks at different transient sizes.

| Molecule | Transient | Observed m/z | Theoretical m/z | ppm error |
|---|---|---|---|---|
| Pheophytin *a* $[M+H]^+$ | 4M | 871.5793850 | 871.573198 | 7.10 |
| Pheophytin *a* $[M+H]^+$ | 8M | 871.5695133 | 871.573198 | -4.23 |
| Pheophytin *a* $[M+H]^+$ | 16M | 871.5742559 | 871.573198 | 1.21 |

Such behavior is in agreement with the general FT-ICR principle that both resolution and mass accuracy benefit from longer transient acquisitions, as the positioning of the peak in the frequency domain can then be determined with higher precision. The shorter 4M transient produces broader peaks and uses a larger digital step size, which makes the exact peak value less stable and therefore increased the deviation from the theoretical mass.

However, the results also show that the relationship is not linear for every peak, which indicates that transient size was not the only factor affecting the measured mass deviation. In FT-ICR MS, mass accuracy is also influenced by aspects such as calibration quality and space-charge effects. In addition, closely spaced or partially overlapping peaks may shift the apparent apex position, especially in crowded spectral regions. The larger deviation observed for some measurements thus likely reflects a combination of peak overlap and inferior peak picking.

Overall, the data suggest that increasing the transient size improved both resolving power and mass accuracy. For the following isotope analysis, this result is integral, providing the

ability to compute isotopic fine structures.

## 5.2 General Observations

The cyanobacterial spectra were first examined visually to determine recurring signals, overall signal intensities and visually prominent ions. Across the dataset, the spectra showed a broad but non-uniform distribution of peaks, with the lower m/z region containing mostly weaker signals while the higher m/z range contained a number of distinct and repeatedly occurring peaks across spectra. The repeated occurrence of the higher m/z signals made that region particularly relevant for further analysis. These peaks were generally stronger, more reproducible between all spectra and more likely to retain visible isotope structures. For this reason, the high mass region became the main focus for both the multivariate comparison and the targeted isotope analysis.

In particular, the signals around m/z 870 were notably higher in intensity, with several fragments identified in the 500-600 m/z region. It was determined to be derivatives of chlorophyll *a*, see figure 5.6, which is the primary photosynthetic pigment in cyanobacteria.

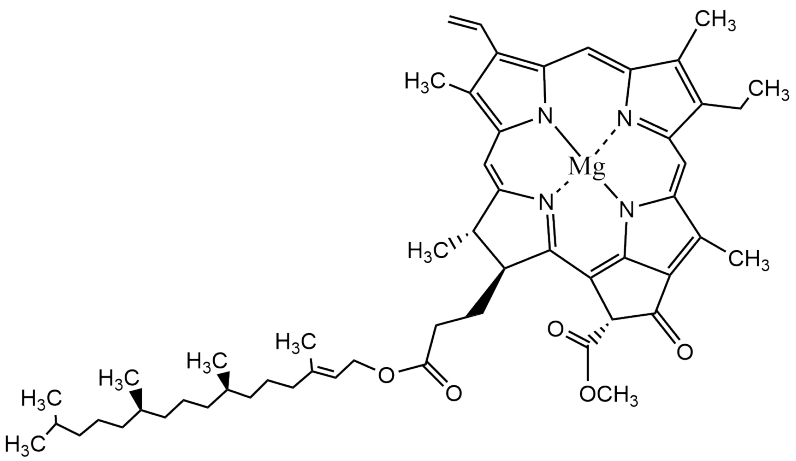


**Figure 5.6:** Chemical structure of chlorophyll-*a*.

However, the analysis of chlorophyll derivatives showed that the cyanobacterial spectra lacked the precense of intact chlorophyll *a*. Instead, the most abundant ion was pheophytin *a*, which is the demetallated form of chlorophyll *a*, thus without the central magnesium (Mg) ion. It was detected as both [M]+ and [M+H]+. Pheophorbide *a* was also detected frequently, which is the pheophytin molecule without the long phytol chain. This indicates that it is difficult to retain the full chlorophyll molecule either during sample preparation, or it experiences demetallation during irradiation or in the ICR cell. Chlorophyll is sensitive to degradation, especially in aqueous media when irradiated, which may prove it difficult to retain the molecular ion using MALDI [42]. This observation is important for interpretation of the later isotope results, because it shows that the dominant high-mass pigment signals in the spectra were not derived from intact chlorophyll alone. Instead, the most intense recurrent peaks were associated with degraded chlorophyll species.

A noteworthy exception was discovered while examining different matrix concentrations, where for some measurements using low concentrations of CHCA matrix provided visible chlorophyll peaks in early measurements. This may indicate that chlorophyll breakdown may occur in the sample overtime, but also that it is sensitive to high energy dispersion in the sample spot. As increasing the concentration of matrix significantly increased signal intensity, it is probable that it results in either demetallation or suppression of chlorophyll in the spectra. These measurements also detected chlorophyllide *a*, which is the chlorophyll *a* molecule without the phytol chain, but with the central Mg atom intact, contrary to pheophorbide. As can be seen in figure 5.1, they also stand out as the only signals detected with comparatively low intensities compared to other measurements, meaning all other molecular information is lost. Another observation is that as the concentration of matrix was increased, the intensity of pheophytin increased substantially, while chlorophyll is not detectable at all.

Other than pigment related compounds some recurrent peaks were related to larger membrane glycolipids such as monogalactosyldiacylglycerol (MGDG), and were identified in the 800 m/z region. As such, through this initial inspection of the mass spectra along with some molecules that can be expected in cyanobacteria, the target formulas later used for isotope analysis was determined, see table 5.3 below [43], [44].

**Table 5.3:** Expected target compounds used for isotope analysis.

| **Target** | **Formula** | **Annotation** |
|---|---|---|
| MGDG 34:4 | $C_{43}H_{74}O_{10}$ | Glycolipid |
| MGDG 34:3 | $C_{43}H_{76}O_{10}$ | Glycolipid |
| MGDG 34:2 | $C_{43}H_{78}O_{10}$ | Glycolipid |
| DGDG 34:3 | $C_{49}H_{86}O_{15}$ | Digalactosyldiacylglycerol |
| DGDG 34:2 | $C_{49}H_{88}O_{15}$ | Digalactosyldiacylglycerol |
| PG 34:3 | $C_{40}H_{73}O_{10}P$ | Phosphatidylglycerol |
| PG 34:2 | $C_{40}H_{75}O_{10}P$ | Phosphatidylglycerol |
| PG 36:5 | $C_{42}H_{73}O_{10}P$ | Phosphatidylglycerol |
| Chlorophyll a | $C_{55}H_{72}MgN_4O_5$ | Chlorophyll pigment |
| Pheophytin a | $C_{55}H_{74}N_4O_5$ | Chlorophyll derivative |
| Pheophorbide a | $C_{35}H_{36}N_4O_5$ | Chlorophyll derivative |
| Chlorophyllide a | $C_{35}H_{34}MgN_4O_5$ | Chlorophyll derivative |
| $\beta$-Carotene | $C_{40}H_{56}$ | Carotenoid |
| Zeaxanthin | $C_{40}H_{56}O_2$ | Carotenoid |
| SQDG 34:2 | $C_{43}H_{78}O_{12}S$ | Sulfoquinovosyldiacylglycerol |
| SQDG 34:4 | $C_{43}H_{74}O_{12}S$ | Sulfoquinovosyldiacylglycerol |

It should be noted that table 5.3 represents the initial screening list used for isotope analysis rather than a list of finally validated identifications. The purpose of these targets was to simplify the analysis of the cyanobacteria by removing the compound identification aspect.

## 5.3 Multivariate Analysis

To evaluate if the mass spectra collected from *Cyanothece* and *Synechocystis* differed from each other, principal component analysis (PCA) was performed. As can be seen in figure

5.7, the two groups had differed mostly in dispersion. Along PC1, the *Cyanothece* spectra were generally shifted toward positive values, while the *Synechocystis* spectra were instead shifted toward negative values. This indicates that the variation in total mass spectra correspond to differentiation in strain. At the same time, the score plot still shows some overlap, suggesting that the two groups shares common spectral background and are not entirely distinct from each other.

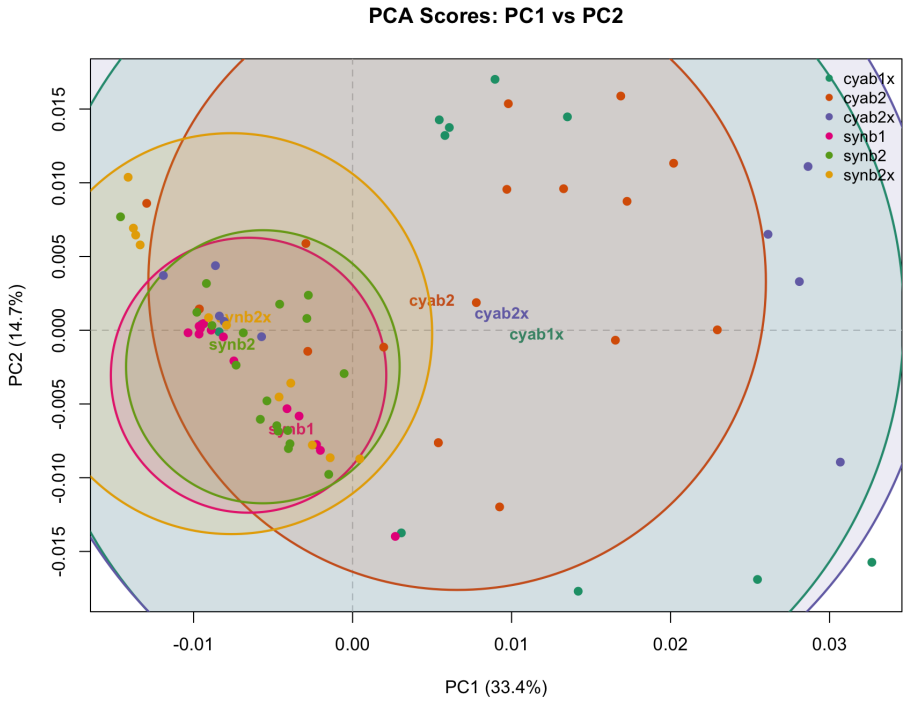


**Figure 5.7:** PCA score plot for two cyanobacteria strains *Cyanothece* and *Synechocystis*, with three cultures each.

There is significant dispersion mainly in the *Cyanothece* spectra, while the three *Synechocystis* cultures remain more clustered. This difference in dispersion is described further in the PCA distance plot, see figure 5.8. It should be noted that PC1 and PC2 together explained 48.06% of the total variance, meaning that a substantial part of the spectral variation is not explained by the two first components. The PCA should therefore not be regarded as a complete description of all spectral differences.

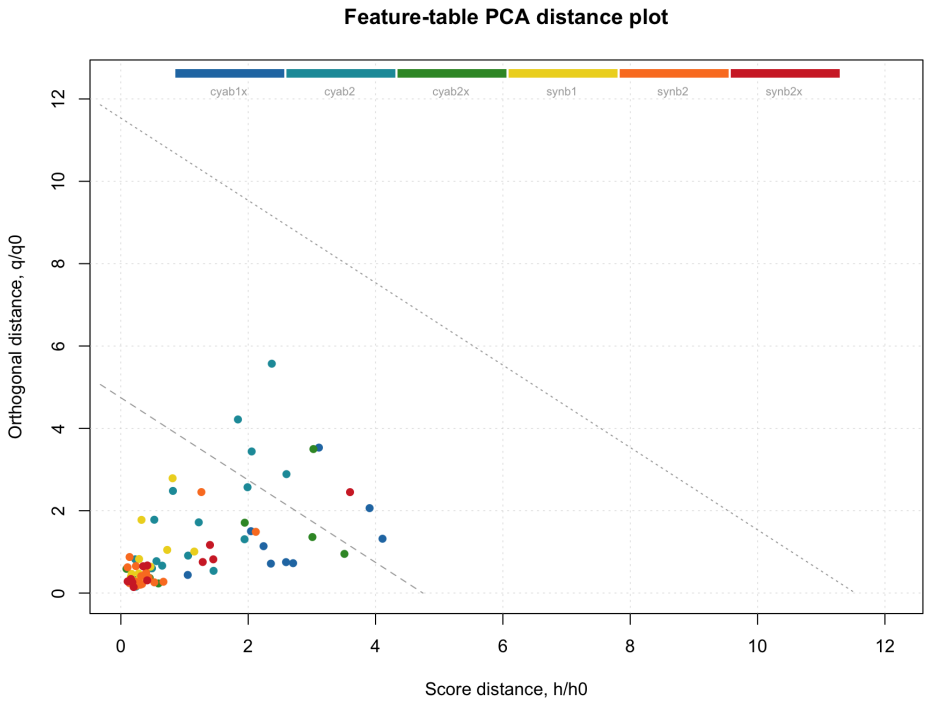


**Figure 5.8:** Visualization of PCA distance plotfor two cyanobacteria strains *Cyanothece* and *Synechocystis*, with three cultures each.

In figure 5.8, the x-axis represents the normalized score distance (h/h0) which represents how far the spectrum lies from the center of the PCA model. The y-axis represents the normalized orthogonal distance (q/q0), which reflects how well the spectrum is fitted by the model. Spectra located near the lower left corner are therefore both typical and well described by the model, while spectra with higher score distance may be considered more extreme or less well fitted. The tendency of the *Cyanothece* spectra to occur at greater score distances indicates that this group was more dispersed around the model center than *Synechocystis*, which may be explained as inconsistencies between replicate spectra.

Figure 5.9 shows the loading plot from the PCA, and indicates that the separation between spectra was driven mainly by features in the 800-900 m/z region. Features such as m/z 871.08, 855.08, 877.09, and 893.04 are on one side of the loading space, while m/z 871.57, 870.57, and 872.58 are located on the opposite side. This indicates that the separation between Cyanothece and Synechocystis was influenced by differences in neighboring signals within the same mass region.

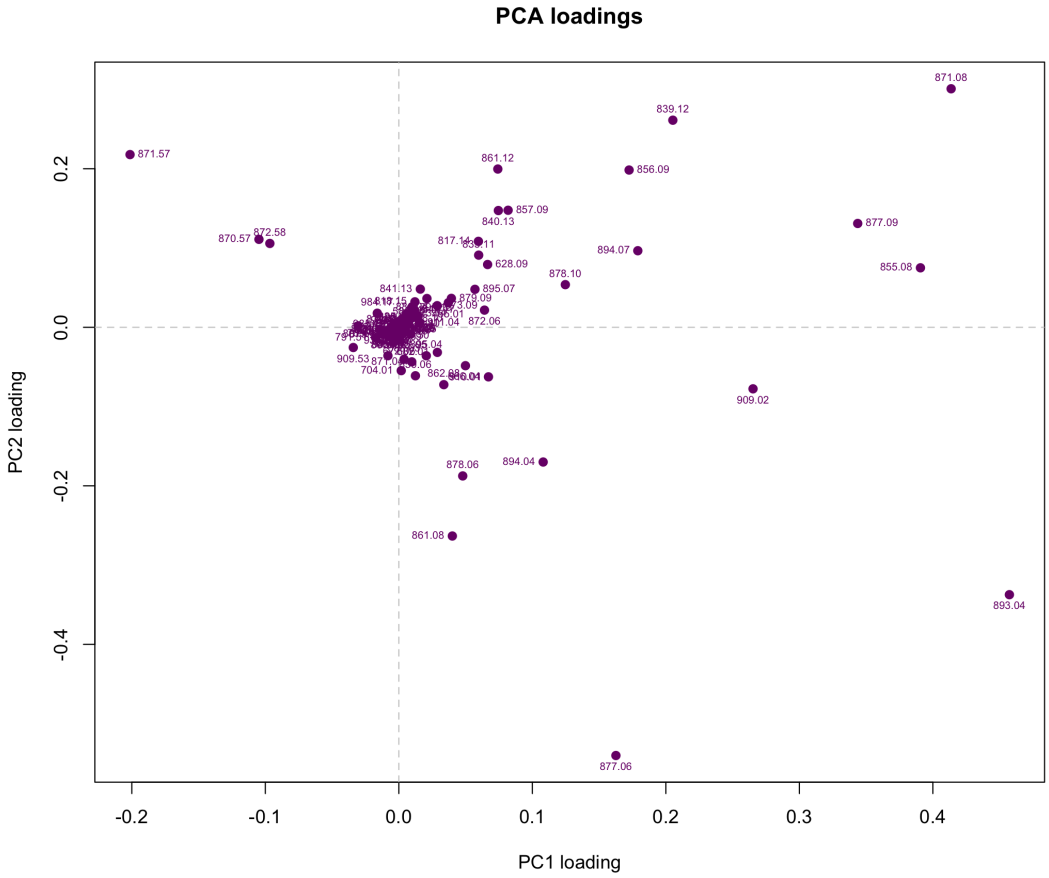


**Figure 5.9:** PCA loading plot for cyanobacteria strains *Cyanothece* and *Synechocystis*.

To quantify the separation, the spectra were individually examined for the features that stood out, by inspecting the presence of the peaks between the strains. For *Synechocystis* a total of 43 spectra were used for PCA, while 39 were used for *Cyanothece*.

**Table 5.4:** Occurrence of selected PCA-associated peaks in *Cyanothece* and *Synechocystis*.

| **m/z** | ***Cyanothece* presence** | ***Synechocystis* presence** |
|---|---|---|
| 855.08 | 25/39 (64.1%) | 32/43 (74.4%) |
| 870.57 | 10/39 (25.6%) | 13/43 (30.2%) |
| 871.08 | 33/39 (84.6%) | 11/43 (25.6%) |
| 871.57 | 10/39 (25.6%) | 24/43 (55.8%) |
| 872.58 | 9/39 (23.1%) | 15/43 (34.9%) |
| 877.06 | 15/39 (38.5%) | 28/43 (65.1%) |
| 877.09 | 22/39 (56.4%) | 2/43 (4.7%) |
| 893.04 | 26/39 (66.7%) | 34/43 (79.1%) |
| 909.02 | 26/39 (66.7%) | 10/43 (23.3%) |

The feature at m/z 871.08 is notable, since it is much more abundant in *Cyanothece* than in *Synechocystis*. The opposite trend was observed for m/z 871.57, which was higher in *Synechocystis*. By contrast, the prominent peak at m/z 870.57 was not significantly different between the two groups. The feature at $m/z$ 909.02 was also strongly enriched in

*Cyanothece*.

For the features with similar peak presence, comparisons between mean normalized intensities of the peaks was done to examine the effect on the PCA. Table 5.5 presents the results. In this table, normalized intensity means that each spectrum was first scaled to a common total signal level before comparison. The values therefore describe how much each peak contributes to the normalized spectrum on average, rather than its absolute raw intensity.

**Table 5.5:** Mean sum-normalized intensities for selected peaks with similar occurrence in *Cyanothece* and *Synechocystis*. Intensities are expressed as percentages of the total normalized spectral signal.

| **m/z** | **Mean *Cyanothece*(%)** | **Mean *Synechocystis*(%)** | **Dominant strain** |
|---|---|---|---|
| 855.08 | 1.192 | 0.317 | *Cyanothece* |
| 870.57 | 0.445 | 0.592 | *Synechocystis* |
| 872.58 | 0.251 | 0.472 | *Synechocystis* |
| 893.04 | 1.173 | 0.375 | *Cyanothece* |

Table 5.5 shows that across peaks with similar occurrence in both strains, present differences in intensity. The signals at m/z 855.08 and 893.04 show higher mean normalized intensities in *Cyanothece*, while m/z 870.57 and 872.58 are more intense in *Synechocystis*. Together, the peak-presence and peak-intensity comparisons suggest that the PCA separation may be driven by both factors. Some features differed mainly because they occurred more frequently in one strain than in the other, while other features were detected in both strains but showed different mean signal intensities. This may indicate that the factors driving variance between the strains was influenced by both peak occurrence in the spectra and differences in peak intensity.

This can be explained as both real biochemical differences or as the result of different responses to the ionization. Cyanobacterial membranes are known to be dominated by the lipid classes MGDG, DGDG, SQDG and PG, and the relative abundance of these membrane lipids can vary depending on the growth conditions [43]. Pigment composition is also not constant across cyanobacteria, as the relative abundance of chlorophyll *a* and carotenoids such as $\beta$-carotene and zeaxanthin may differ between strains [44]. It is therefore possible that the balances of abundances may be altered in *Cyanothece* and *Synechocystis*. At the same time, MALDI peak intensity is not determined by analyte abundance alone, but also by ion suppression and space charge effects. The observed PCA separation and the differences in peak intensity are thus most likely explained by a combination of true variation between the strains and ionization effiency.

## 5.4 Isotope Analysis

This section will present the results of the isotope identification in the cyanobacterial samples. The total analysis was comprised of two parts, firstly the general visibility of isotope patterns in regard to the presence of $M$, $M+1$, and $M+2$ peaks. These regions were then evaluated as by the combined isotope contributions relative to the parent peak, in order to determine whether a clear overall isotope pattern was present. Secondly, these same

regions were examines to determine if it was possible to resolve isotopic fine structures. It is important to note that all results in this section is based on measurements with a minimum resolution of 500,000.

### 5.4.1 Isotope Patterns

The isotope analysis was successful for a substantial portion of the targeted molecular formulas in table 5.3. The final screening recovered a total of 68 parent monoisotopic peaks, where 43 passed the validation criteria. Overall, the most prominent set of isotope patterns was from pheophytin *a*, along with the corresponding adducts [M+H]+ and [M+Na]+. Several additional chlorophyll related compounds were also recovered, such as chlorophyllide, pheophorbide as well as some Mg-containing chlorophyll fragments at m/z 481 and 555. However the most consistent results were obtained for the pheophytin ions, as it was typically the most abundant ion. As such, the results are henceforth focused on the pheophytin region for isotope ratios.

The mass accuracy of the validated parent assignments was mostly acceptable, with a mean parent mass error of about 1.35 ppm. However, the results also show that the identification of validated parent ions did not guarantee a visible isotope pattern. Several ions found no validated isotopes, indicating that isotope pattern investigation depend not only on presence of accurate mass peaks, but also signal intensity and peak overlap. Hence, the isotope patterns results are visible only for the ions that have the combination of high abundance and high peak resolution.

**Table 5.6:** Mass accuracies for select validated parent ions.

| **Target** | **Adduct** | **Theoretical m/z** | **Observed m/z** | **ppm error** |
|---|---|---|---|---|
| Pheophytin a | [M+H]+ | 871.573198 | 871.574256 | 1.214 |
| Pheophytin a | [M+Na]+ | 893.555142 | 893.556595 | 1.625 |
| SQDG 34:4 | [M+K]+ | 853.453257 | 853.452172 | -1.271 |
| MGDG 34:3 | [M+K]+ | 791.507007 | 791.508346 | 1.693 |
| PG 36:5 | [M+Na]+ | 791.483356 | 791.482293 | -1.343 |

Pheophytin *a* [M+H]+ and [M+Na]+ gave the clearest overall isotope patterns. The protonated ion was observed at m/z 871.5742559 with a mass error of 1.21 ppm compared to the theoretical value, and the sodium adduct ion at m/z 893.5565946 with a mass error of 1.63 ppm. Additionally the isotope patterns of both ions were highly consistent with the excpected theoretical pattern.

For pheophytin [M+H]+, the combined $M+1$ region corresponded to 52.57% of the parent intensity, while the combined $M+2$ region corresponded to 14.62%. For pheophytin [M+Na]+, the corresponding values were 46.29% for the combined M+1 region and 15.88% for the combined M+2 region. The direct comparisons to expected values can be seen in table 5.7. Thus, both adducts displayed a relatively strong isotope pattern.

**Table 5.7:** Observed and expected combined isotope intensities for pheophytin *a* adducts.

| Adduct | Exp. M+1 (%) | Obs. M+1 (%) | Exp. M+2 (%) | Obs. M+2 (%) |
|---|---|---|---|---|
| [M+H]+ | 60.50 | 52.57 | 19.01 | 14.62 |
| [M+Na]+ | 60.50 | 46.29 | 19.01 | 15.88 |

However, the sodium adduct of pheophytin showed a weaker intensity ratio than for [M+H]+, in the same measurement. Since the isotopic composition of a molecule should not depend on adduct form, this is unlikely to be due to an actual chemical difference. A possible explanation could be that, as the [M+Na]+ parent ion was weaker in signal, it may be more affected by local overlap. As can be seen in figure 5.10, the region includes several other peaks near the proposed isotope peaks.

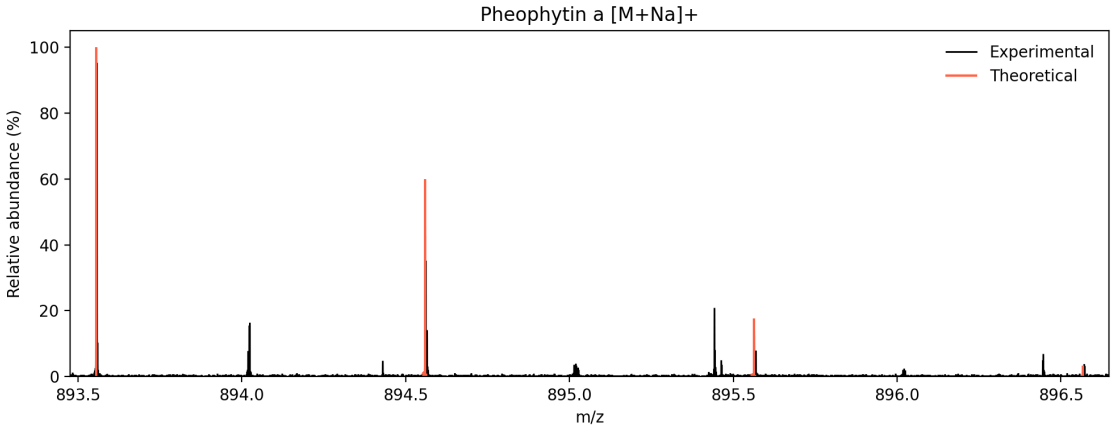


**Figure 5.10:** Simulated spectra of [M+Na]+ region for pheophytin *a*.

The isotope ratios were also compared across all spectra, and for the pheophytin-related adducts, the degree of reproducibility differed between strains. The isotope ratios for the *Synechocystis* spectra generally showed lower spread than *Cyanothece*. This was most evident for the $^{13}$C contribution of pheophytin [M+H]+, which gave a mean ratio of 0.527 with a standard deviation of 0.064 in *Synechocystis*, compared with 0.589 and 0.156 in *Cyanothece*. This indicates a $\pm 6.4\%$ standard deviation in the $M+1$ peak for *Synechocystis*, while it is $\pm 15.6\%$ for *Cyanothece*. Hence, the ratio analysis suggests that the measurements on *Synechocystis* had a much more stable isotope pattern, while *Cyanothece* showed greater spectral heterogeneity and thus lower reproducibility. This interpretation is also consistent with the PCA results, where *Cyanothece* showed greater dispersion than *Synechocystis*. For the $M+2$ isotope ratios, not enough measurements with high resolution showed valid isotopes, thus making the comparison unreliable.

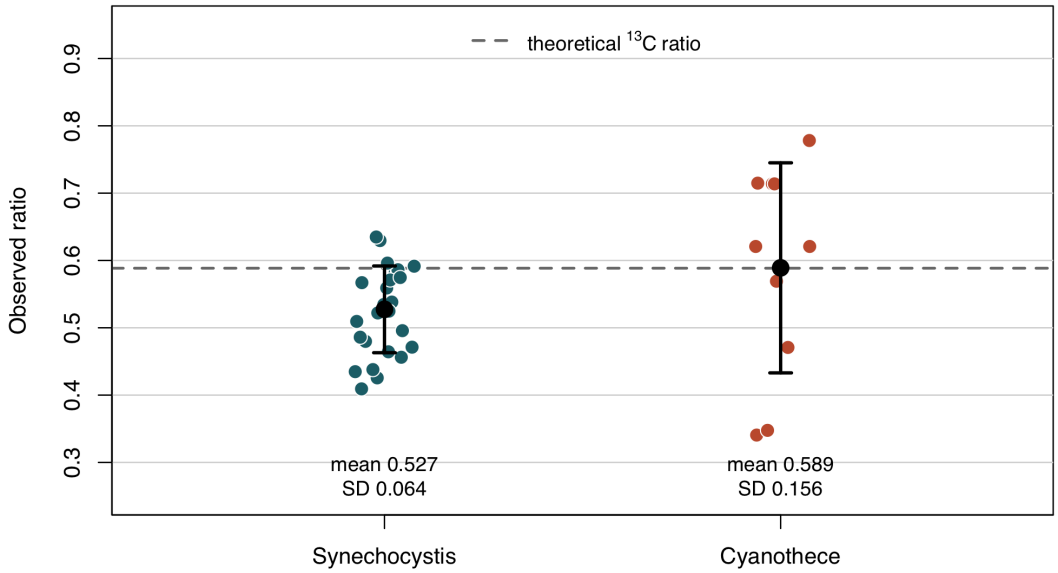


**Figure 5.11:** Reproducibility test for intensity ratio of carbon isotope contributions in $M+1$.

As it was noted that intensities in the $M+1$ region could vary substantially during data analysis, additional screening was performed. When examined visually in the spectrum, some measurements showed the signal as two close peaks, while in others it was dominated by a single main peak instead. This indicates that the $M+1$ region may not always represent one isotope peak, but can instead contain overlapping contributions. This case is especially prominent for [M]+ ions compared to the corresponding [M+H]+ ions, where the mass difference between the $^{13}$C isotopologue of the [M]+ ion and the monoisotopic [M+H]+, is very small. The difference is approximately 0.00447 Da, but is resolved when using the highest resolution measurements. This is possibly the reason for the appearance of a double-peak in the $M+1$ peak, as well as variation in the intensity ratios across measurements.

This is important for interpretation of isotope patterns, because the intensity of the $M+1$ region may then depend not only on the presence of isotopes, but also on other overlapping contributions. Thus, comparison between many measurements using solely data analysis should be interpreted cautiously, since overlap between neighboring peaks can influence the calculated isotope ratios. A possible improvement of the current workflow would therefore be to add additional validation of the isotope peaks, by searching for specific adduct contributions in close vicinity that may cause this overlap.

### 5.4.2 Isotopic Fine Structure

Following the initial evaluation of the overall isotope patterns, the validated $M+1$ and $M+2$ regions were examined further. Individual contributions in the regions were resolved and assigned based on comparison with the theoretical fine structure pattern. In total,

689 theoretical fine structure candidates were generated, of which 191 were detected in the experimental data, while 73 were validated. The mass accuracy of the fine structure assignments were high, with a mean of 0.1096 ppm. Thus, the peaks that could be resolved and validated had observed masses close to the expected theoretical positions.

Of note is the fact that all isotope assignments were made on raw MS data, with minimum preprocessing applied. Thus, no aligning or binning of clusters was performed in order to reduce the loss of isotope data.

The clearest and most complete fine-structure results were obtained for pheophytin. For the protonated ion, [M+H]+, the $M+1$ region could be resolved into a dominant $^{13}C$ contribution at m/z 872.577712 together with a small $^{15}N$ contribution at m/z 872.571379. The patterns are visualized in plots including the expected theoretical placements compared to the found experimental values, see figure 5.12. It is worth noting that the experimental peaks are shifted according to the ppm error with which the parent ion was found.

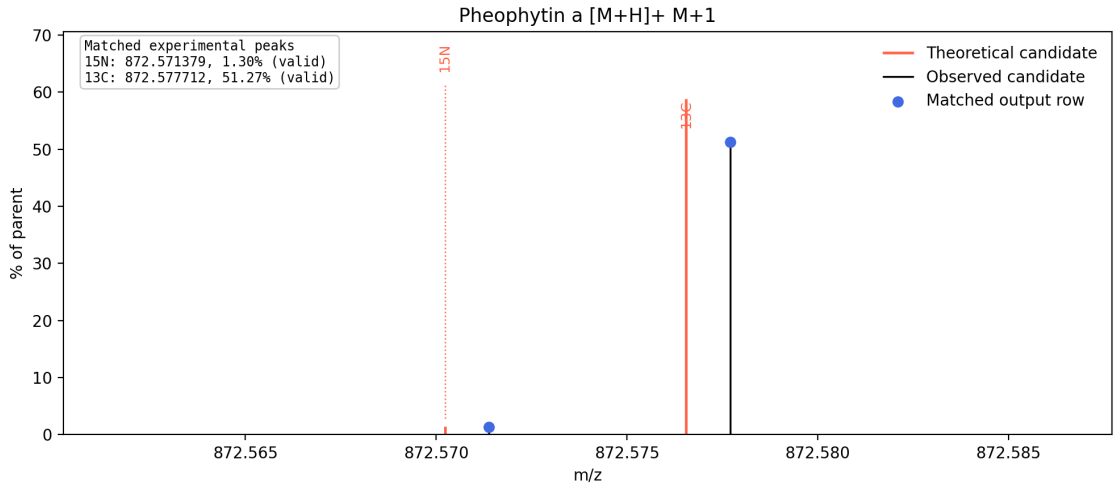


**Figure 5.12:** Isotopic fine structure comparison between theoretical pattern and found observed values, for $M+1$ peak of pheophytin.

In the $M+2$ region, the strongest validated component was $^{13}C_2$ at m/z 873.581153 and a $^{18}O$ contribution at m/z 873.578403. In figure 5.13, a contribution from $^{15}N$+$^{13}C$ was also found, but did not pass validation.

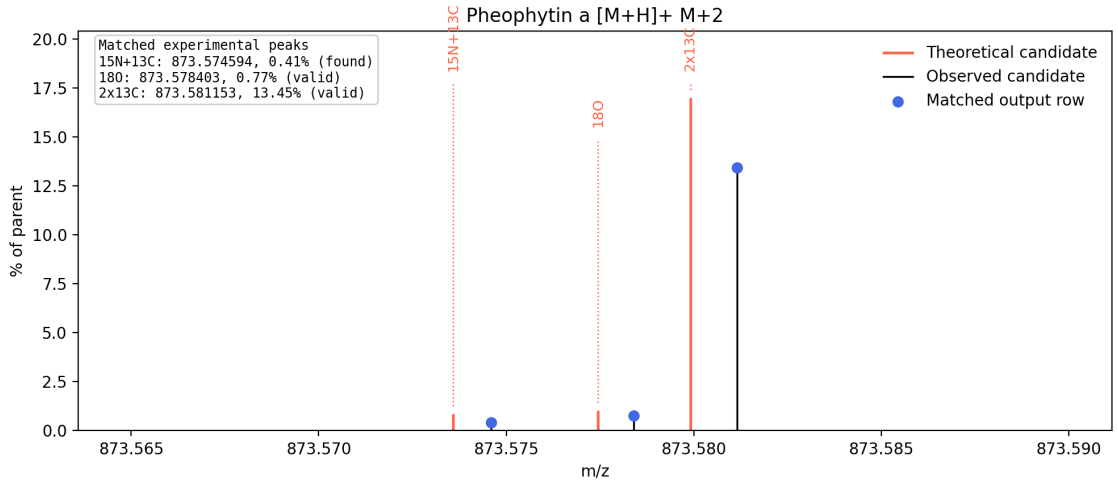


**Figure 5.13:** Isotopic fine structure comparison between theoretical pattern and found observed values, for $M + 2$ peak of pheophytin.

Fine-structure information was not restricted to pheophytin. Several additional ions showed interesting resolved isotope structures. Among the lipids, SQDG 34:4 was particularly notable as a fine structure containing sulfur was detected. For SQDG 34:4 [M+K]+, the validated assignments included $^{13}$C in the $M + 1$ peak as well as a small $^{33}$S contribution that did not pass validation.

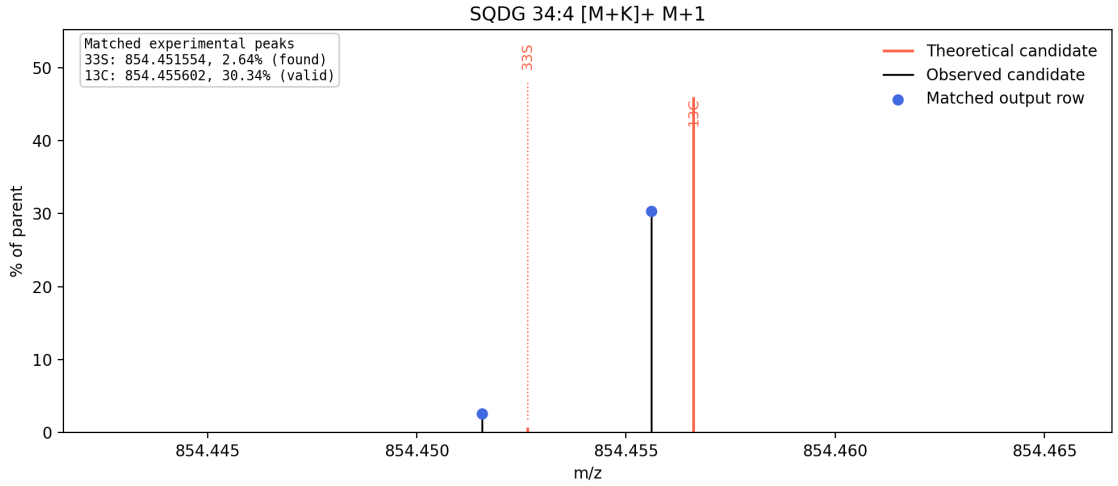


**Figure 5.14:** Isotopic fine structure comparison between theoretical pattern and found observed values, for $M + 1$ peak of SQDG 34:4.

In the M+2 region, $^{13}C_2$, $^{18}$O and $^{34}$S was observed. The $^{33}$S $+^{13}$C contribution was found but not validated, similarly to the $^{33}$S in the $M + 1$ peak.

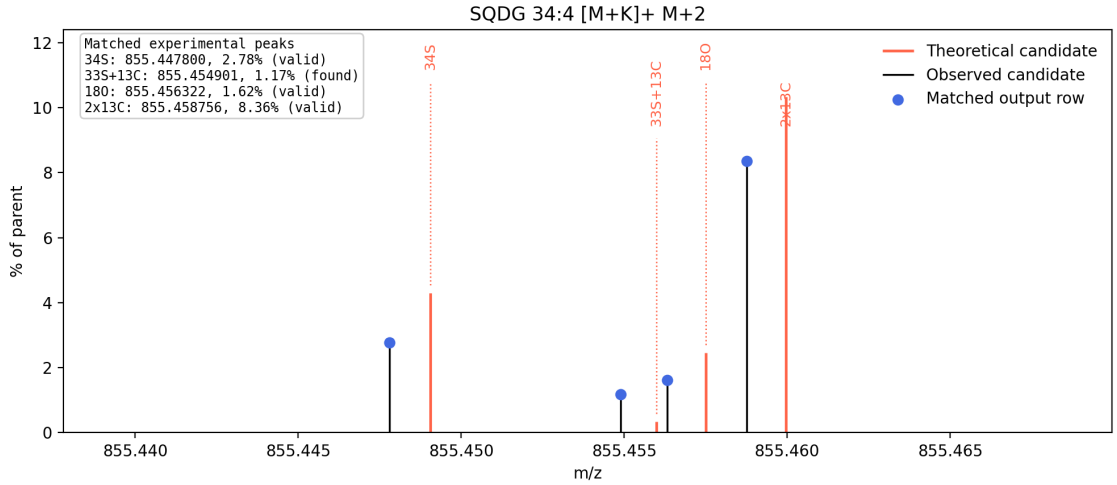


**Figure 5.15:** Isotopic fine structure comparison between theoretical pattern and found observed values, for $M + 2$ peak of SQDG 34:4.

Magnesium fine structures were also observed in some chlorophyll-derived ions. However, the parent ions were typically lower in intensity, making it difficult to detect contribution from less abundant isotopes. Chlorophyllide showed a $^{25}$Mg in the M+1 region, but no valid isotopes for M+2. Several chlorophyll fragments showed found isotopes for $^{26}$Mg, however none passed validation. Most of them failed due to the mass error being above the set limit.

The distribution of validated assignments was dominated by carbon components. Among the 73 validated candidates, 36 corresponded to $^{13}$C and 19 to $^{13}C_2$, while other contributions were less frequent. This distribution is consistent with the expectation that carbon atoms are abundant in most organic molecules.

The results demonstrate the existence of limitations in the MALDI spectra of complex samples. Not all theoretical components were recovered, and not all detected peaks could be retained after validation, especially for low intensity or crowded regions. For example, some expected low abundance contributions in pheophytin were detected but not validated, and minor oxygen containing peaks were similarly excluded despite being visually present. The failed validation of these signals may not indicate that the isotopic contribution does not exist, but rather that the spectral collection was insufficient for confident assignment.

The fine structure results therefore support the conclusion that the measurements have high enough quality to move beyond isotope pattern identification, and instead also resolve individual isotopic contributions. However, it is also noticable that the assignments depended strongly on local signal intensity, spectral complexity and the degree of overlap within the isotope cluster.

An interesting further application of this workflow is the possibility of using the isotopic fine structure in reverse to the present result. That is, to determine the elemental composition of unknown compounds in the spectra. If the fine structure of the isotope regions can be resolved, this provides information of individual contributions from for example $^{13}$C, $^{15}$N and $^{18}$O. By combining exact mass values and then examining abundances of isotopes,

potential molecular formulas of unknown mass peaks can be narrowed down significantly. Thus, it may help with distinguishing between candidate formulas that otherwise have similar monoisotopic masses. In this way, isotope-based analysis could potentially be used not only for validation of known targets, but also for annotation of unknown peaks in complex mass spectra.

# 6

# Conclusions and Future Outlook

This project presented that MALDI FT-ICR MS can be used to investigate isotope patterns and isotopic fine structures in cyanobacteria. The most informative results were obtained for pheophytin ions, specifically [M+H]+ and [M+Na]+, which showed good agreement with theoretical patterns. The overall comparison between the two strains *Cyanothece* and *Synechocystis*, showed that the two strains were chemically distinguishable, while still sharing a common spectral background. The separation was related mainly to recurring mass features as well as the individual intensity differences between spectra.

For the isotope patterns, the results showed that $M+1$ and $M+2$ peak clusters could be recovered using data analysis, for some targeted membrane lipids and chlorophyll derivatives. More detailed fine structure analysis showed that the isotope peaks were dominated mainly by carbon related contributions, while other isotopes such as oxygen and sulfur could also be resolved in some cases. The study also showed that interpretation of isotopic fine structures remained strongly dependent on local peak overlap and peak resolution. Increasing the transient size improved resolving power and thus made it possible to recover the contributions. However, complete determination was not always achieved in crowded regions.

Future work should focus on strengthening the validation of observed isotope patterns. Importantly, the study would benefit from comparison with standards, or samples with differences in treatment or exposure. Future studies should also optimize the balance between resolution and acquisition efficiency, for example by using high-resolution acquisition only in specific mass range windows. As such, it would improve the computational efficiency.

Overall, this work demonstrates that MALDI FT-ICR MS is a suitable instrument for isotope analysis while requiring minimal preparation, and with the possibility of performing high-throughput analysis.

# References


[1] Z. Muccio and G. P. Jackson, "Isotope ratio mass spectrometry," *Analyst*, vol. 134, no. 2, pp. 213–222, Feb. 2009, ISSN: 13645528. DOI: 10.1039/B808232D.

[2] M. Wiggenhauser, R. E. Moore, P. Wang, G. P. Bienert, K. H. Laursen, and S. Blotevogel, "Stable Isotope Fractionation of Metals and Metalloids in Plants: A Review," *Frontiers in Plant Science*, vol. 13, p. 840 941, Apr. 2022, ISSN: 1664462X. DOI: 10.3389/FPLS.2022.840941/FULL.

[3] J. B. West, G. J. Bowen, T. E. Cerling, and J. R. Ehleringer, "Stable isotopes as one of nature's ecological recorders," *Trends in Ecology & Evolution*, vol. 21, no. 7, pp. 408–414, Jul. 2006, ISSN: 0169-5347. DOI: 10.1016/J.TREE.2006.04.002.

[4] X. Zhou, M. P. Taylor, H. Salouros, and S. Prasad, "Authenticity and geographic origin of global honeys determined using carbon isotope ratios and trace elements," *Scientific Reports 2018 8:1*, vol. 8, no. 1, pp. 14 639–, Oct. 2018, ISSN: 2045-2322. DOI: 10.1038/s41598-018-32764-w.

[5] E. Oras, S. Vahur, S. Isaksson, I. Kaljurand, and I. Leito, "MALDI-FT-ICR-MS for archaeological lipid residue analysis," *Journal of Mass Spectrometry*, vol. 52, no. 10, pp. 689–700, Oct. 2017, ISSN: 1096-9888. DOI: 10.1002/JMS.3974.

[6] C. A. Crutchfield and W. Clarke, "Present and Future Applications of High Resolution Mass Spectrometry in the Clinic," *Discoveries*, vol. 2, no. 2, e17, Jun. 2014. DOI: 10.15190/d.2014.9.

[7] F. Pingitore, Y. Tang, G. H. Kruppa, and J. D. Keasling, "Analysis of Amino Acid Isotopomers Using FT-ICR MS," *Analytical Chemistry*, vol. 79, no. 6, pp. 2483–2490, Mar. 2007, ISSN: 00032700. DOI: 10.1021/AC061906B.

[8] G. L. Glish and R. W. Vachet, "The basics of mass spectrometry in the twenty-first century," *Nature Reviews Drug Discovery*, vol. 2, no. 2, pp. 140–150, Feb. 2003, ISSN: 14741776. DOI: 10.1038/NRD1011;KWRD.

[9] H. Awad, M. M. Khamis, and A. El-Aneed, "Mass spectrometry, review of the basics: Ionization," *Applied Spectroscopy Reviews*, vol. 50, no. 2, pp. 158–175, Feb. 2015, ISSN: 1520569X. DOI: 10.1080/05704928.2014.954046;WGROUP:STRING:PUBLICATION.

[10] E. d. Hoffmann and V. Stroobant, *Mass spectrometry : principles and applications*. Chichester: J. Wiley, 2007, vol. 3, ISBN: 9780470033104.

[11] C. Bhardwaj and L. Hanley, "Ion sources for mass spectrometric identification and imaging of molecular species," *Natural Product Reports*, vol. 31, no. 6, pp. 756–767, May 2014, ISSN: 14604752. DOI: 10.1039/C3NP70094A.

[12] K. Dreisewerd, "The Desorption Process in MALDI," *Chemical Reviews*, vol. 103, no. 2, pp. 395–425, Feb. 2003, ISSN: 00092665. DOI: 10.1021/CR010375I.

[13] R. Knochenmuss, "Fundamentals of MALDI," in *Electrospray and MALDI Mass Spectrometry: Fundamentals, Instrumentation, Practicalities, and Biological Applications*, R. B. Cole, Ed., 2nd ed., Hoboken, NJ.: Wiley, 2010, ch. 5, pp. 149–245, ISBN: 9780471741077.

[14] R. Knochenmuss, "An Introduction to MALDI Ionization Mechanisms for Users of Mass Spectrometry Imaging," pp. 1–19, Nov. 2021. DOI: 10.1039/9781839165191-00001.

[15] I. C. Lu, "A thermal perspective on MALDI ionization: A long journey from fundamental mechanisms to a practical solution for carbohydrate analysis," *International Journal of Mass Spectrometry*, vol. 518, p. 117 516, Dec. 2025, ISSN: 13873806. DOI: 10.1016/j.ijms.2025.117516.

[16] Y.-H. Lai and Y.-S. Wang, "Matrix-Assisted Laser Desorption/Ionization Mass Spectrometry: Mechanistic Studies and Methods for Improving the Structural Identification of Carbohydrates," *Mass Spectrometry*, vol. 6, no. Spec Iss 2, S0072, 2017, ISSN: 2187-137X. DOI: 10.5702/MASSSPECTROMETRY.S0072.

[17] R. Knochenmuss and R. Zenobi, "MALDI Ionization: The Role of In-Plume Processes," *Chemical Reviews*, vol. 103, no. 2, pp. 441–452, Feb. 2002, ISSN: 00092665. DOI: 10.1021/cr0103773.

[18] R. Knochenmussa and L. V. Zhigilei, "Molecular dynamics simulations of MALDI: laser fluence and pulse width dependence of plume characteristics and consequences for matrix and analyte ionization," *Journal of mass spectrometry : JMS*, vol. 45, no. 4, pp. 333–346, 2010, ISSN: 1096-9888. DOI: 10.1002/JMS.1732.

[19] A. M. Haag, "Mass analyzers and mass spectrometers," *Advances in Experimental Medicine and Biology*, vol. 919, pp. 157–169, 2016, ISSN: 22148019. DOI: 10.1007/978-3-319-41448-5{_}7/FIGURES/8.

[20] F. Xian, C. L. Hendrickson, and A. G. Marshall, "High Resolution Mass Spectrometry," *Analytical Chemistry*, vol. 84, no. 2, pp. 708–719, Jan. 2012, ISSN: 00032700. DOI: 10.1021/AC203191T.

[21] Y. Qi and P. B. O'Connor, "Data processing in Fourier transform ion cyclotron resonance mass spectrometry," *Mass Spectrometry Reviews*, vol. 33, no. 5, pp. 333–352, Sep. 2014, ISSN: 10982787. DOI: 10.1002/mas.21414.

[22] J. P. Savaryn, T. K. Toby, and N. L. Kelleher, "A Researcher's Guide to Mass Spectrometry-Based Proteomics," *Proteomics*, vol. 16, no. 18, p. 2435, Sep. 2016, ISSN: 16159861. DOI: 10.1002/PMIC.201600113.

[23] A. G. Marshall, C. L. Hendrickson, and G. S. Jackson, "Fourier transform ion cyclotron resonance mass spectrometry: A primer," *Mass Spectrometry Reviews*, vol. 17, no. 1, pp. 1–35, 1998, ISSN: 02777037. DOI: 10.1002/(SICI)1098-2787(1998)17:1<1::AID-MAS1>3.0.CO;2-K.

[24] M. Maia, A. Figueiredo, C. Cordeiro, and M. Sousa Silva, "FT-ICR-MS-based metabolomics: A deep dive into plant metabolism," *Mass Spectrometry Reviews*, vol. 42, no. 5, pp. 1535–1556, Sep. 2023, ISSN: 1098-2787. DOI: 10.1002/MAS.21731.

[25] A. G. Marshall and C. L. Hendrickson, "Fourier transform ion cyclotron resonance detection: principles and experimental configurations," *International Journal of Mass Spectrometry*, vol. 215, no. 1-3, pp. 59–75, Apr. 2002, ISSN: 1387-3806. DOI: 10.1016/S1387-3806(01)00588-7.

[26] D. Cochran and R. Powers, "Fourier Transform Ion Cyclotron Resonance Mass Spectrometry Applications for Metabolomics," *Biomedicines*, vol. 12, no. 8, p. 1786, Aug. 2024, ISSN: 22279059. DOI: 10.3390/BIOMEDICINES12081786/S1.

[27] C. G. Dekoster, M. C. Duursma, G. J. Vanrooij, *et al.*, "Routine Part-per-Million Mass Accuracy for High- Mass Ions: Space-Charge Effects in MALDI FT-ICR," *Analytical Chemistry*, vol. 71, no. 3, pp. 624–632, Feb. 1998, ISSN: 00032700. DOI: 10.1021/AC980690D.

[28] U. M. Hohenester, P. Barbier Saint-Hilaire, F. Fenaille, and R. B. Cole, "Investigation of space charge effects and ion trapping capacity on direct introduction ultra-high-resolution mass spectrometry workflows for metabolomics," *Journal of Mass Spectrometry*, vol. 55, no. 10, e4613, Oct. 2020, ISSN: 1096-9888. DOI: 10.1002/JMS.4613.

[29] A. Rossmann, "DETERMINATION OF STABLE ISOTOPE RATIOS IN FOOD ANALYSIS," *Food Reviews International*, vol. 17, no. 3, pp. 347–381, 2001, ISSN: 87559129. DOI: 10.1081/FRI-100104704.

[30] W. Meier-Augenstein, *Stable isotope forensics : an introduction to the forensic application of stable isotope analysis*. Wiley-Blackwell, 2010, vol. 3, ISBN: 9780470517055.

[31] A. L. Buchachenko, "Mass-Independent Isotope Effects," *Journal of Physical Chemistry B*, vol. 117, no. 8, pp. 2231–2238, Feb. 2013, ISSN: 15205207. DOI: 10.1021/JP308727W.

[32] T. Ishida, "Isotope effect and isotope separation: A chemist's view," *Journal of Nuclear Science and Technology*, vol. 39, no. 4, pp. 407–412, 2002, ISSN: 00223131. DOI: 10.1080/18811248.2002.9715214.

[33] M. H. Thiemens, "Introduction to chemistry and applications in nature of mass independent isotope effects special feature," *Proceedings of the National Academy of Sciences of the United States of America*, vol. 110, no. 44, pp. 17 631–17 637, Oct. 2013, ISSN: 00278424. DOI: 10.1073/PNAS.1312926110.

[34] T. B. Coplen, "Guidelines and recommended terms for expression of stable-isotope-ratio and gas-ratio measurement results," *Rapid Communications in Mass Spectrometry*, vol. 25, no. 17, pp. 2538–2560, Sep. 2011, ISSN: 1097-0231. DOI: 10.1002/RCM.5129.

[35] P. Dittwald, D. Valkenborg, J. Claesen, A. L. Rockwood, and A. Gambin, "On the Fine Isotopic Distribution and Limits to Resolution in Mass Spectrometry," *Journal of The American Society for Mass Spectrometry 2015 26:10*, vol. 26, no. 10, pp. 1732–1745, Aug. 2015, ISSN: 1879-1123. DOI: 10.1007/S13361-015-1180-4.

[36] *Atomic Weights and Isotopic Compositions for All Elements*. [Online]. Available: https://physics.nist.gov/cgi-bin/Compositions/stand_alone.pl.

[37] F. S. Midani, M. L. Wynn, and S. Schnell, "The importance of accurately correcting for the natural abundance of stable isotopes," *Analytical biochemistry*, vol. 520, p. 27, Mar. 2017, ISSN: 10960309. DOI: 10.1016/J.AB.2016.12.011.

[38] G. Alves, A. Y. Ogurtsov, and Y. K. Yu, "Molecular Isotopic Distribution Analysis (MIDAs) with Adjustable Mass Accuracy," *Journal of The American Society for Mass Spectrometry 2013 25:1*, vol. 25, no. 1, pp. 57–70, Nov. 2013, ISSN: 1879-1123. DOI: 10.1007/S13361-013-0733-7.

[39] P. Kaur and P. B. O'Connor, "Quantitative Determination of Isotope Ratios from Experimental Isotopic Distributions," *Analytical Chemistry*, vol. 79, no. 3, pp. 1198–1204, Feb. 2007, ISSN: 00032700. DOI: 10.1021/AC061535Z.

[40] S. Kucheryavskiy, "mdatools – R package for chemometrics," *Chemometrics and Intelligent Laboratory Systems*, vol. 198, p. 103 937, Mar. 2020, ISSN: 0169-7439. DOI: 10.1016/J.CHEMOLAB.2020.103937.

[41] M. K. Łacki, D. Valkenborg, and M. P. Startek, "IsoSpec2: Ultrafast Fine Structure Calculator," *Analytical Chemistry*, vol. 92, no. 14, pp. 9472–9475, Jul. 2020, ISSN: 15206882. DOI: 10.1021/ACS.ANALCHEM.0C00959.

[42] S. Petrović, J. Zvezdanović, and D. Marković, "Chlorophyll degradation in aqueous mediums induced by light and UV-B irradiation: An UHPLC-ESI-MS study," *Radiation Physics and Chemistry*, vol. 141, pp. 8–16, Dec. 2017, ISSN: 0969-806X. DOI: 10.1016/J.RADPHYSCHEM.2017.05.024.

[43] W. Hewelt-Belka, Á. Kot-Wasik, P. Tamagnini, and P. Oliveira, "Untargeted Lipidomics Analysis of the Cyanobacterium Synechocystis sp. PCC 6803: Lipid Composition Variation in Response to Alternative Cultivation Setups and to Gene Deletion," *International Journal of Molecular Sciences 2020, Vol. 21, Page 8883*, vol. 21, no. 23, p. 8883, Nov. 2020, ISSN: 1422-0067. DOI: 10.3390/IJMS21238883.

[44] B. Wojtasiewicz and J. Stoń-Egiert, "Bio-optical characterization of selected cyanobacteria strains present in marine and freshwater ecosystems," *Journal of Applied Phycology 2016 28:4*, vol. 28, no. 4, pp. 2299–2314, Jan. 2016, ISSN: 1573-5176. DOI: 10.1007/S10811-015-0774-3.

# A

# Appendix

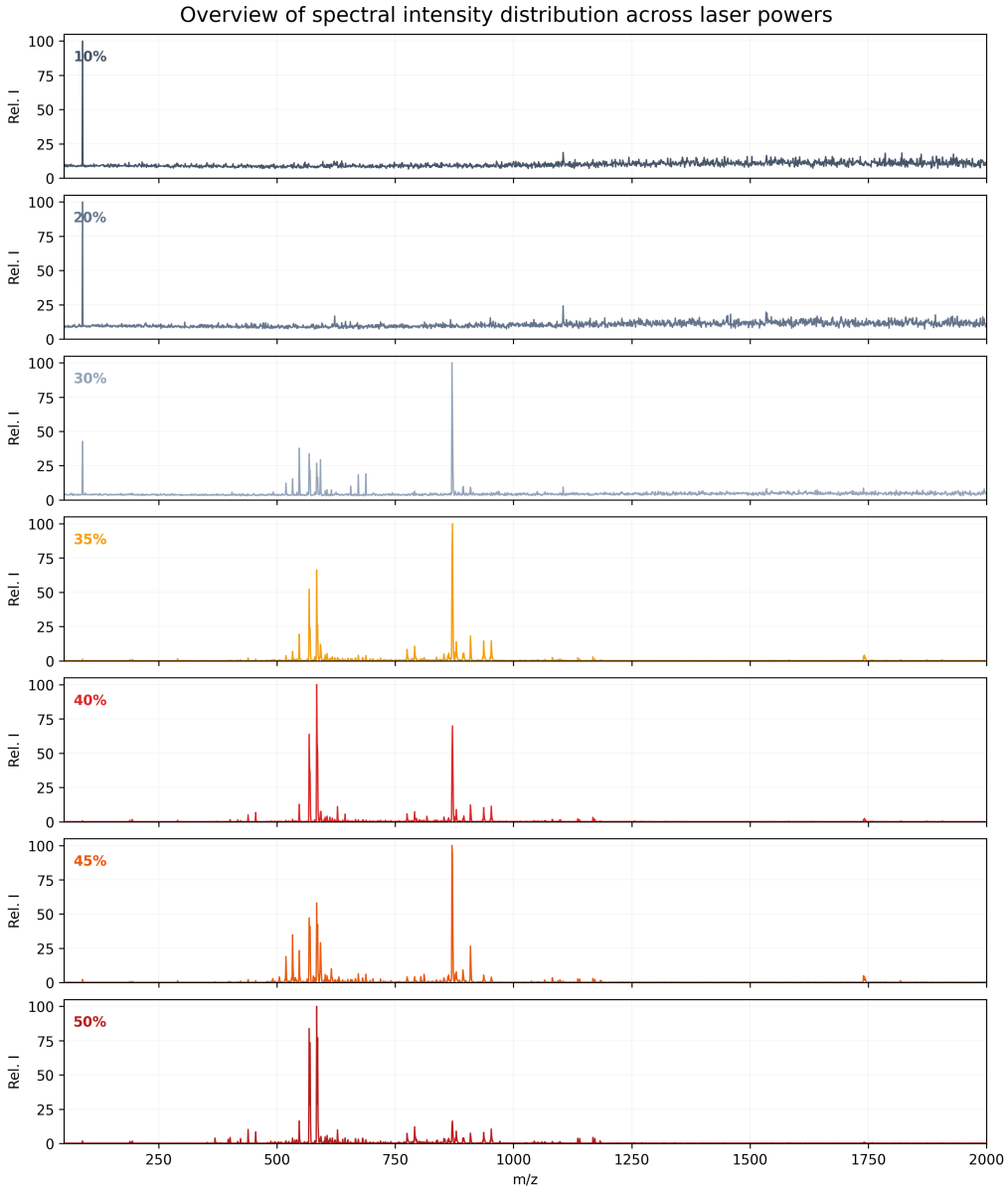


**Figure A.1:** Overview of processed spectra with varying laser power.

**DEPARTMENT OF CHEMISTRY AND CHEMICAL ENGINEERING**
**CHALMERS UNIVERSITY OF TECHNOLOGY**
Gothenburg, Sweden
www.chalmers.se




CHALMERS
UNIVERSITY OF TECHNOLOGY